



Experimental investigation of turbulent and laminar flow regimes in a supersonic free jet under near-vacuum conditions

Han June Park¹ , Sung-Gwang Lee¹ and Wontae Hwang¹ 

¹Department of Mechanical Engineering, Seoul National University, Seoul 08826, Korea

Corresponding author: Wontae Hwang, wthwang@snu.ac.kr

(Received 5 July 2024; revised 22 April 2025; accepted 16 May 2025)

Supersonic free jets are extensively employed across a range of applications, especially in high-tech industries such as semiconductor processing and aerospace propulsion. Due to the difficulties involved in flow measurement, previous research on supersonic free jets has primarily focused on investigating near-field shockwave structures, with quantitative experimental analysis of the far-field zone being relatively scarce. However, physical understanding of the far-field flow, particularly post-shockwave energy dissipation, holds significant importance for the application and utilisation of these jets in vacuum environments. Therefore, this study aims to provide a robust experimental foundation for a rarefied supersonic free jet through the analysis of the flow field in both the near- and far-field zones. Nanometre-sized tracer particles and molecules were utilised to measure the rarefied supersonic jet flow field using particle image velocimetry and acetone molecular tagging velocimetry, respectively. The experiments revealed that in rarefied conditions, the supersonic jet exhibits a one-barrel shockwave structure in the near field, and after passing the Mach disk, a long annular viscous layer develops downstream. Experimental data on the jet velocity profile and width demonstrated a transition to a laminar flow regime in the far-field zone. This transition aligns with the theoretically inferred flow regimes based on the complex Reynolds number. The velocity profile and potential core length of the laminar flow regime could be modelled using a bi-modal distribution, which represents the summation of symmetric Gaussian distributions.

Key words: supersonic flow, jets, shock waves

1. Introduction

As technology advances, the semiconductor and aerospace industries increasingly require an understanding of flow physics at rarefied conditions. In semiconductor fabrication

environments, many processes, including the use of free-jets, occur under vacuum conditions to enhance deposition efficiency, plasma generation and purity. Historically, the understanding of fluid flow in vacuum conditions focused mainly on the overall gas concentration within the processing equipment, allowing operation without a detailed understanding of the flow structure. However, as these processes have become more sophisticated and miniaturised, achieving desired yields without a thorough understanding of the flow dynamics has become increasingly difficult. Consequently, there is a growing demand for insights into the flow physics that governs semiconductor fabrication processes, but the challenges of measuring flows under rarefied conditions often make this difficult to achieve. Research exists for the internal flows within semiconductor manufacturing facilities, such as chemical vapour deposition (CVD) systems, but since experimental investigations are challenging, most studies have relied on continuum computational fluid dynamics (CFD) simulations (Hash *et al.* 2000; Setyawan *et al.* 2002; Li *et al.* 2019). The absence of experimental results raises concerns regarding the validity of the CFD. Issues such as wafer defects caused by nano-particles, which differ significantly from those in atmospheric pressure conditions, are also prominent in rarefied environments (Loth *et al.* 2021; Capecelatro & Wagner 2024).

In outer space environments, spacecraft including satellites typically employ small rocket engines (thrusters) to eject high-temperature or high-pressure exhaust gases (plumes) at supersonic speeds through nozzles, to facilitate precise attitude and orbit control. In the vacuum of space, the internal flow within rocket nozzles transitions from a continuum to a rarefied flow regime (Sukesan & Shine 2023). Consequently, the exhaust gas particles disperse not only downstream of the rocket nozzle, but also in many other directions and in a non-equilibrium state. In such instances, backflow of exhaust gases towards the spacecraft can result in disturbance forces/torques and thermal loads, in addition to causing contamination as the cold surfaces of the spacecraft adsorb these particles (Dettleff & Grabe 2011). Aside from thrusters, there are issues related to plume and surface interactions during spacecraft landings on planetary bodies, which differ from interactions that occur in Earth atmospheric conditions (Plemmons *et al.* 2008; Mehta *et al.* 2013; Silwal *et al.* 2024). However, due to experimental limitations, most studies rely on the direct simulation Monte Carlo (DSMC) method (Bykov, Gorbachev & Fyodorov 2023; Bajpai, Bhateja & Kumar 2024), which is the numerical method for low-density flows where the continuum assumption breaks down.

Even though free jets are frequently employed, research into their behaviour in rarefied environments has predominantly been conducted using computational methods. Some experimental studies have been conducted using electron-beam-induced radiation emission or laser-induced fluorescence (LIF) techniques, primarily for visualisation and concentration analyses (Volchkov *et al.* 1973; Inman *et al.* 2008; Dubrovin *et al.* 2023). Most of these studies have focused on the shockwave structures in the near-field zones of nozzles, and have typically been more qualitative than quantitative in nature.

A non-intrusive quantitative flow measurement technique using acetone as a tracer was first implemented in a rarefied free jet by Lempert *et al.* (2002). Subsequently, various researchers have utilised acetone molecular tagging velocimetry (MTV) to conduct studies on high-speed rarefied free jets (Lempert *et al.* 2003; Huffman & Elliott 2009; Handa *et al.* 2011, 2014; Sakurai *et al.* 2015). Alternative measurement techniques have also been employed, such as Raman spectroscopy for temperature (Tejeda *et al.* 1996; Mate *et al.* 2001; Graur *et al.* 2004) and schlieren imaging for density (Ragheb *et al.* 2010; Schröder *et al.* 2011). However, research has generally been limited to phenomena in the near-field zones, such as the zone of silence and the Mach disk.

In practical applications such as semiconductor CVD chambers and spacecraft nozzles, the far-field zone of jets plays a critical role due to its influence on various interactions and processes. In semiconductor manufacturing, the far-field zone governs the dynamics of CVD, where uniform material deposition depends on precise control of jet behaviour to ensure accurate delivery to the substrate. Similarly, in spacecraft propulsion, micro-throttles used for fine attitude control rely on the far-field zone to determine exhaust plume characteristics, impacting the stability and efficiency of operations under low-pressure conditions (Dettleff 1991; Sukesan & Shine 2023). Additionally, during spacecraft lift-off and landing, plume-surface interactions dominate, particularly in retropropulsion systems that create complex multiphase flow environments (Mehta *et al.* 2013; Gorman *et al.* 2023; Rodrigues, Tyrrell & Danehy 2024; Cuesta *et al.* 2025). Understanding the dynamics of the far-field zone is essential for designing safe and efficient landing systems on Martian or lunar surfaces. Theoretically, as the flow becomes more rarefied, it transitions into a stable state with diminished flow properties fluctuations (Garcia *et al.* 1987; Mansour *et al.* 1987; Yang & Huang 1995; Stefanov, Boyd & Cai 2000). While this phenomenon has been observed qualitatively through LIF (Inman *et al.* 2008), turbulence effects may persist, highlighting the need for quantitative analysis in the far-field zone, which remains under-explored in the literature. Moreover, supersonic jets naturally form in these environments due to extremely low ambient pressures, where the total-to-ambient pressure ratio often exceeds the critical nozzle pressure ratio (NPR) 1.8, as predicted by isentropic relations. This results in inevitable supersonic flow, emphasising the necessity of studying their behaviour to optimise applications in both semiconductor processing and space exploration.

Therefore, the objective of this study is to conduct a comprehensive experimental analysis of the flow structure of a rarefied supersonic free jet across both near- and far-field zones, in order to provide a deeper understanding of the flow physics involved. As the jet becomes more rarefied, its flow characteristics evolve, transitioning through turbulent and laminar flow regimes depending on the ratio between total and ambient pressures, Reynolds number and Knudsen number. The remainder of this paper is organised as follows. In § 2, we review the relevant main parameters of a jet as it exits the nozzle at a supersonic speed and interacts with the surrounding environment. In § 3, the experimental set-up of the custom-designed vacuum chamber and measurement uncertainties for the particle image velocimetry (PIV) and acetone MTV techniques are provided. In § 4, experimental results and theoretical modelling of the velocity profiles are explained. Finally, in § 5, a summary and conclusions are given.

2. Characterisation of jet rarefaction

For a sonic nozzle, the structure of shockwaves in a supersonic free jet is essentially influenced by the NPR η_0 , which is defined as the ratio of total (P_0) to ambient (P_∞) pressure. Depending on the NPR, the supersonic free jet may exhibit behaviours in the over-expanded or under-expanded regimes.

In the over-expanded regime, the exit pressure of the jet is less than the ambient pressure. This leads to a series of compression shocks within the jet as it adjusts to the higher ambient pressure. These shocks are typically followed by expansion fans, creating a complex pattern of alternating shocks and expansions. Conversely, the under-expanded regime occurs when the exit pressure is higher than the ambient pressure. The jet undergoes expansion waves as it adjusts to the lower external pressure, resulting in a visible spreading of the flow.

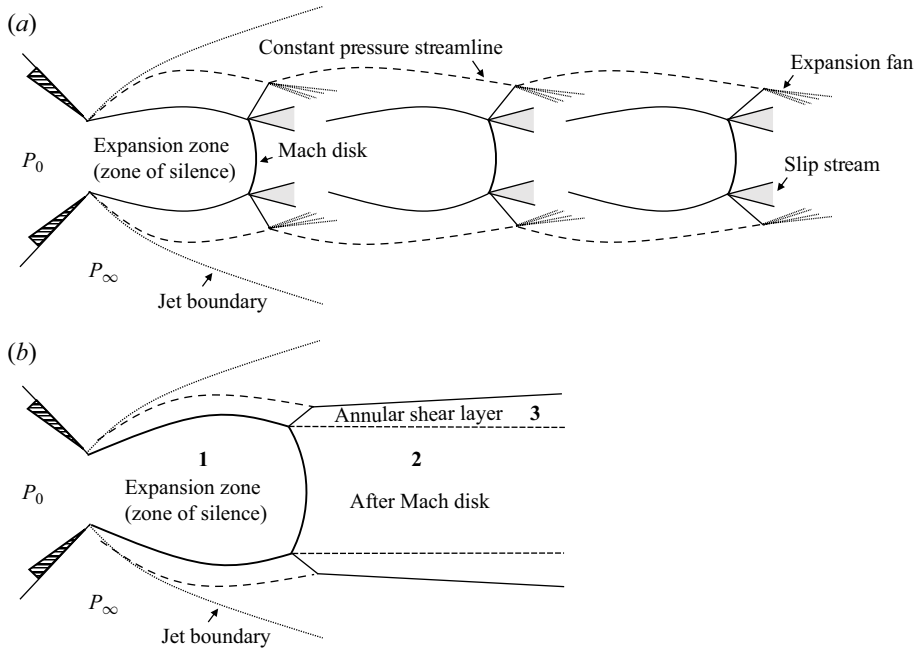


Figure 1. Schematic of flow structure in (a) a highly under-expanded and (b) an extremely under-expanded supersonic free jet.

The under-expanded regime can be further divided into different subdivisions based on the magnitude of the pressure difference and corresponding flow characteristics, as depicted in figure 1. The basic under-expanded condition involves a mild series of expansions as the jet slightly adjusts to achieve equilibrium with the ambient pressure. As the pressure difference becomes more pronounced, there is a shift to a moderately or highly under-expanded regime, where intense and clearly defined shock diamonds or Mach disks appear, signifying substantial pressure adjustments through strong shockwaves followed by expansion waves. The extremely under-expanded regime features a large single shock cell or a Mach disk near the nozzle exit, followed by a long potential core and highly turbulent flow that significantly spreads the jet profile as it progresses downstream. In this study, due to the high pressure difference between the jet and the rarefied environment, we focus on the highly under-expanded jet characterised by the presence of a Mach disk and cyclical structures due to oblique shockwaves, and the extremely under-expanded regime where only a single-barrel shock structure exists.

Additionally, especially in a rarefied gas environment, it is important to consider both the NPR and the jet rarefaction factor, which depends on the Reynolds, Mach and Knudsen numbers. Previous research (Volchkov *et al.* 1973; Kislyakov, Rebrov & Sharafutdinov 1975; Kosov, Rebrov & Sharafutdinov 1980; Rebrov 2001; Bykov *et al.* 2023) highlights the fact that the Reynolds number alone is not sufficient to fully describe the flow behaviour under rarefied conditions. This has led to the conceptualisation of a complex Reynolds number (Volchkov *et al.* 1973), denoted as Re_L , which is defined as the Reynolds number at the nozzle throat, divided by the NPR:

$$Re_L = Re_* / \sqrt{\frac{P_0}{P_\infty}} = Re_* / \sqrt{\eta_0}, \quad (2.1)$$

where Re_* is the Reynolds number based on the nozzle throat diameter, P_0 is total pressure, P_∞ is ambient pressure, and η_0 is the NPR, respectively. In this study, Re_* was calculated using the jet velocity at the exit of the sonic nozzle, where the flow is choked. The jet velocity was determined using isentropic relations, as choking implies that the flow reaches Mach 1 at the exit. Using the known total pressure and total temperature, the static temperature under choked conditions was calculated with isentropic relations. The speed of sound, and thus the jet velocity, was then derived using the static temperature and a constant specific heat ratio. Furthermore, the corresponding complex Knudsen number (Dulov & Luk'yanov 1984), denoted as Kn_L , is given as

$$Kn_L = \frac{\lambda_\infty}{L} \sim \frac{1}{Re_L}, \quad (2.2)$$

where λ_∞ is the mean free path of molecules in the ambient gas, and L is the characteristic length scale.

The formulation of the complex Reynolds number incorporates not just the NPR but also principal parameters from key regions in the extremely under-expanded supersonic free jet, as illustrated in [figure 1\(b\)](#). These regions are delineated into three main areas: the zone of silence before the Mach disk (region 1), the area following the Mach disk (region 2), and the annular shear layer unaffected by the Mach disk (region 3). By calculating the Reynolds number with characteristic density, length, velocity and viscosity from each of these regions, the composite nature of the complex Reynolds number becomes evident, as detailed in [Appendix A](#). The complex Reynolds number not only elucidates the characteristics of the near-field zone of the supersonic free jet, but also describes the far-field zone. Typically, as the jet reaches the far-field zone, it becomes fully developed, satisfying self-similarity conditions and is known to exhibit a Gaussian velocity profile.

The complex Reynolds number is used to differentiate flow characteristics, and the following distinctions represent each flow regime (Rebrov 2001): turbulent for $Re_L > 10^4$, laminar–turbulent transition for $10^3 < Re_L < 10^4$, laminar for $10^2 < Re_L < 10^3$, and rarefied or scattering for $Re_L < 10^2$. The current research focuses on examining how the characteristics of the supersonic free jet change under rarefied conditions, investigating a highly under-expanded jet in the turbulent flow regime and an extremely under-expanded jet in the laminar flow regime.

3. Experimental set-up

3.1. Vacuum chamber

The vacuum chamber developed for this work is shown in [figure 2](#). The cylindrical chamber dimensions are length 835 mm, outer diameter 365 mm, and inner diameter 304 mm. It features optical windows 130 mm × 550 mm in size on three sides to facilitate laser illumination and excitation for PIV and MTV, respectively, and for camera imaging. In this study, a target flow rate 5 standard litres per minute and chamber pressure 1 torr were set, which is relevant to semiconductor equipment and similar to the Mars atmosphere. Two vacuum pressure gauges (numbered 2 and 3) were installed upstream and downstream to measure the internal pressure, as shown in [figure 2\(a\)](#). These sensors were placed sufficiently far from the jet outlet – at least 10 nozzle diameters away – to avoid disturbances caused by the jet flow. A Leybold SV-300B rotary vane vacuum pump was used in combination with a Leybold WS1001 booster to continuously evacuate the chamber. The vacuum pump was placed at the outlet with a throttle valve for pressure control. A control box adjusted the valve based on pressure readings from the gauges. Thermocouples were utilised to monitor temperature directly on the chamber walls to

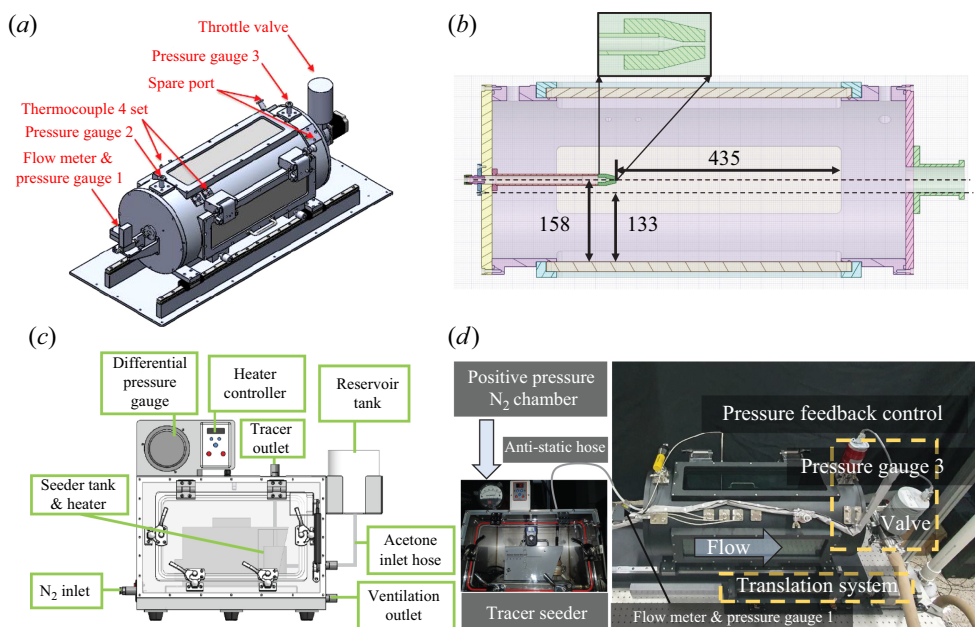


Figure 2. Experimental set-up: (a) vacuum chamber, (b) top view cross-section of vacuum chamber (measurements in mm), (c) tracer seeder within positive pressure N_2 chamber, (d) overall system.

track ambient conditions, and upstream near the nitrogen reservoir to ensure accurate readings of total temperature. Both measurements confirmed uniform total temperature 300 K. As illustrated in [figure 2\(b\)](#), the nozzle is positioned 158 mm from the side optical windows, and 435 mm from the right-hand side of the window. A converging sonic nozzle with a 2 mm capillary orifice, designed per Murphy & Miller (1984), was used to achieve Mach 1 at the exit. This design ensured flow stability, theoretical validation of centreline properties, and minimal wall and outlet influence on the free jet. A motorised translation stage was installed to enable movement of the entire vacuum chamber relative to the optics. It allowed for a translation range of 300 mm along the longitudinal axis, with spatial resolution 100 μm .

However, due to the sudden pressure drop that occurs in the expansion zone near the sonic nozzle outlet, an additional pressure gauge 1 (SMC ZSE30AF-01-C) and flow meter (SMC PFM710S-01-D) were installed between the chamber and the tracer seeder to determine total pressure and flow rate, respectively, as shown in [figure 2\(a\)](#). The total pressure was measured using upstream pressure gauge 1, located before the flow entered the chamber, ensuring an accurate total pressure measurement unaffected by chamber dynamics.

A positive pressure N_2 chamber was installed adjacent to the vacuum chamber to facilitate tracer seeding, thereby removing the possibility for O_2 quenching of phosphorescence in the MTV experiments, and ensuring that large external particles do not enter the seeder in the PIV experiments. As shown in [figure 2\(c\)](#), the N_2 chamber features an inlet for ultra-pure dry N_2 to enter. The seeder was a TSI aerosol generator (model 3079A) for injecting NaCl nano-particles for PIV, and acetone nano-droplets for MTV. Additionally, a side reservoir tank was equipped to continuously supply fluid to the seeder tank. To ensure temperature stability after acetone vaporisation cooling, the seeder tank was heated and controlled by a heater controller. An O_2 sensor was installed inside the positive pressure N_2 chamber to verify that the O_2 concentration was

Flow regime	Turbulent (continuum)	Laminar (continuum)
Chamber pressure (P_∞)	10 torr	1 torr
Total pressure (P_0)	121 torr	128 torr
Chamber temperature (T_∞)	300 K	300 K
Total temperature (T_0)	300 K	300 K
Outlet Mach number	1	1
Critical (outlet) Reynolds number (Re_*)	4.53×10^3	4.53×10^3
Complex Reynolds number (Re_L)	1.30×10^3	4.00×10^2
Critical (outlet) Knudsen number (Kn_*)	2.94×10^{-4}	2.94×10^{-4}
Complex Knudsen number (Kn_L)	7.67×10^{-4}	2.94×10^{-3}
Stokes number (Cunningham correction)	0.089	0.089

Table 1. Overall experimental conditions.

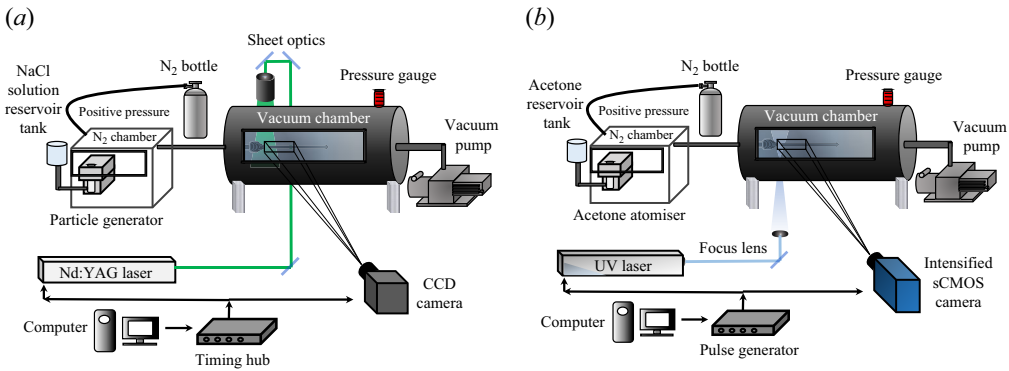


Figure 3. Experimental set-up for (a) PIV and (b) MTV and LIF.

negligible. Connections between the chambers used anti-static hoses to prevent particle agglomeration. The overall configuration of the vacuum chamber and pump set-up is shown in figure 2(d). The overall experimental conditions are detailed in table 1. The fluid thermophysical properties required for calculating these parameters were obtained from the NIST Standard Reference Database (Linstrom *et al.* 2005), with detailed information provided in Appendix B.

3.2. Particle image velocimetry (PIV)

A schematic of the set-up for the PIV experiments is shown in figure 3(a). The system consisted of a dual-cavity 200 mJ pulse⁻¹ 532 nm Nd:YAG laser with frequency 15 Hz. The laser sheet was oriented such that it passed vertically through the vacuum chamber. Images were acquired using a dual-frame 12 bit CCD camera (VH-4MC-M20A0) with 2048×2048 pixel² equipped with a 105 mm macro lens at f/2.8, for a region of interest (ROI) measuring 40×40 mm². The vacuum chamber was capable of longitudinal movement up to 300 mm, which allowed for precise selection of the measurement region. Image stitching was employed to obtain an aggregate overall velocity field.

The PIV flow tracers were NaCl particles, chosen for their low ($\sim 0.5 \times$) density compared to other solid tracer particles. Nano-particles were generated using a 0.001 mol aqueous solution of NaCl in the aerosol generator. These particles were atomised

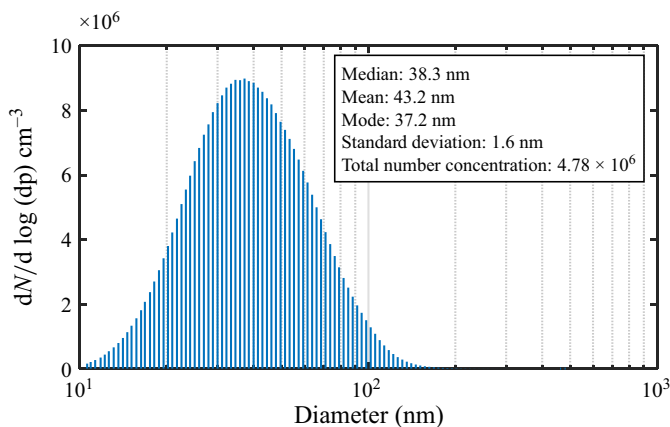


Figure 4. The NaCl solid particle size distribution.

into droplets, which upon evaporation left NaCl solutes that were used as seed particles. Sufficient length of the tube leading into the vacuum chamber was ensured to allow complete evaporation of the droplets into NaCl particles. The size distribution of these particles was diagnosed using a TSI scanning mobility particle sizer (SMPS) model 3938, and the results are given in [figure 4](#). The average size of the particles was approximately 40 nm.

Considering the particle size, which is smaller than the laser wavelength, the scattering regime can be classified as Rayleigh scattering rather than Mie scattering. These particles act as a solid-phase carrier within the nitrogen gas phase. Due to their size and composition, the scattering intensity from the nano-particles is several orders of magnitude greater than that of the surrounding nitrogen. Consequently, the primary signal captured by the camera is dominated by the nano-particles. The captured signal distributions closely resemble typical PIV images rather than those of molecular Rayleigh scattering.

The time interval between successive PIV images was controlled using an IDT MotionPro timing hub that has 100 ns temporal resolution, and was adjusted according to the free jet velocity. Nanosecond intervals were used in the near-field zone (i.e. a high-speed region), while microsecond intervals were used in the far-field zone where the velocity was decaying. Over 500 image pairs were captured for each ROI and analysed using PIVlab (Stamhuis & Thielicke 2014). The final interrogation window size was 32×32 pixel² with 50% overlap due to the wide dynamic range of velocity. All experimental parameters related to the PIV set-up are summarised in [table 2](#).

3.3. Molecular tagging velocimetry (MTV) and laser-induced fluorescence (LIF)

The MTV technique does not rely on tracer particles but directly measures the flow velocity using gas molecules. This method inherently avoids issues related to flow traceability present in PIV, as it measures velocity not indirectly through tracer particles, but directly through gas molecules. Common tracer molecules include acetone, biacetyl and toluene, which are used based on their emission characteristics and the environmental conditions of the experiment. In this study, acetone was utilised.

The basic MTV measurement method seeds the molecular tracers into the flow. When exposed to an appropriate ultraviolet (UV) laser, acetone molecules undergo excitation, and emit light at a different wavelength when returning to the ground state. This light

Laser intensity	200 mJ pulse ⁻¹
Laser wavelength	532 nm
Acquisition rate	15 Hz
Camera resolution	2048 × 2048 px ²
Region of interest (ROI)	40 × 40 mm ²
Final interrogation window size	32 × 32 px ² with 50 % overlap
Tracer particle	Solid NaCl
Number of image pairs per set	> 500 pairs
Number of stitched ROI windows	10 torr, six ROI windows; 1 torr, six ROI windows

Table 2. The PIV system parameters.

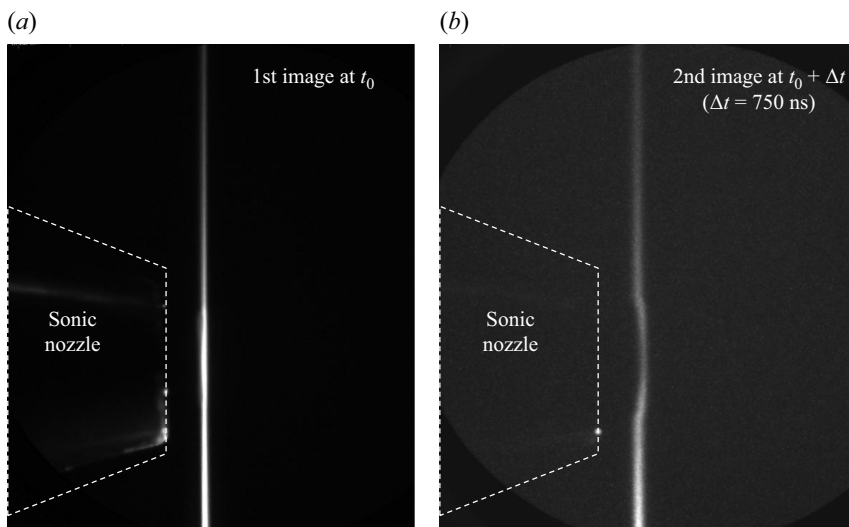


Figure 5. Example of successive MTV images at 1 torr: (a) first image, and (b) second image.

emission can occur in two forms: fluorescence and phosphorescence. Fluorescence occurs in extremely short times of the order of nanoseconds, but with high intensity, followed by a longer-lasting, lower-intensity phosphorescence. This emission characteristic has been used extensively in rarefied supersonic free jets, with early applications by Lempert *et al.* (2002). The emitted light from the tracer molecules is captured using a high-sensitivity camera recording images at predetermined intervals. By analysing the recorded images as shown in figure 5, the displacement of the tracer molecules over known time intervals can be observed. Lines are drawn in the streamwise direction to perform Gaussian fitting, with the velocity determined based on distance moved of the Gaussian profile peak, as depicted in figure 6(a).

For the MTV experimental set-up, as illustrated in figure 3(b), the same chamber used for PIV was employed. The system consisted of a 60 mJ UV single-pulse laser at 266 nm with frequency 10 Hz. This change was necessary to induce the desired molecular excitation in acetone. It should be noted that the energy output of the lasers (both PIV and MTV) was routinely monitored using optical power meters (Thorlabs PM400 and S470C, respectively) to ensure stability across experiments.

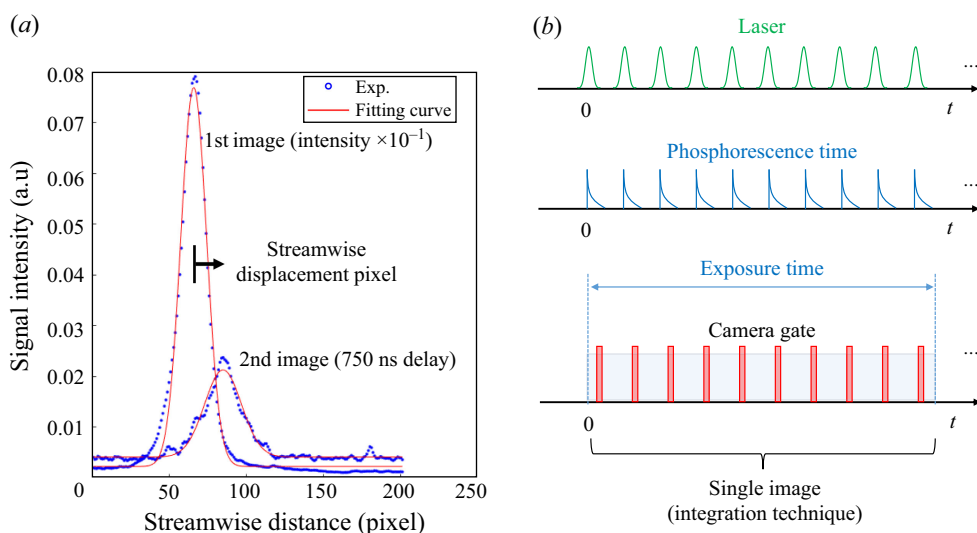


Figure 6. (a) Signal intensity of first image (downscaled by 10^{-1} for visibility) and second image with Gaussian fitting. (b) Signal sequence of MTV using integration technique.

Gaseous acetone was used as the molecular tracer, and was introduced using the same aerosol generator as in the PIV experiment. Upon UV irradiation, both fluorescence and phosphorescence emission at wavelength 405 nm were detected. An intensified 16 bit sCMOS camera (Excelitas pco.dicam C1 P46) was employed with 2048×2048 pixel² equipped with a 200 mm macro lens at f/4, and focused on an ROI measuring 30×30 mm². The camera integration technique developed by Fratantonio *et al.* (2018, 2020) was used in this work. As illustrated in figure 6(b), this technique allows for the capture of light generated by multiple laser excitations in a single image by keeping the camera gate open for a specified duration after each laser irradiation. This method enhanced the signal-to-noise ratio (SNR) by allowing the accumulation of 10 shots per image, synchronised with the 10 Hz frequency of the pulsed UV laser in this experiment.

Unlike in PIV, which captures nano-particle Rayleigh scattering, shutter speed is important for MTV due to the duration of phosphorescence, which is of the order of microseconds. To prevent image streaking and reduce measurement uncertainty, camera gate time 20 ns was used, which is approximately an order of magnitude shorter than the expected phosphorescence duration. This gate time was achieved using a pulse generator (Quantum Composers 9528) with temporal resolution 250 ps. The sequence of UV laser exposure was verified using a 1 ns rise time photodiode (Thorlabs SM05PD2A), connected to a 1 GHz bandwidth oscilloscope (Teledyne LeCroy Wavesurfer 510), to ensure correct timing. A total of 300 image pairs per set were captured using this method. The specific experimental parameters related to the MTV setup are summarised in table 3.

To further elucidate the shockwave structure of the supersonic free jet, acetone LIF was utilised – LIF is particularly effective for visualising shockwave structures because fluorescence intensity is proportional to the acetone concentration, allowing the identification of high-concentration regions within shockwaves (Tropea *et al.* 2007; Inman *et al.* 2008; Yu *et al.* 2013). Unlike MTV, which requires two images for analysis, LIF can be analysed with a single image, making it a more straightforward method. To visualise a wider area, the laser beam is expanded into a broad sheet rather than focused into a single point. This adjustment is easily achieved by replacing the focusing lens used in MTV with a lens that creates a planar laser sheet.

Laser intensity	60 mJ pulse ⁻¹
Laser excitation wavelength	266 nm
Acquisition rate	10 Hz
Camera resolution	2048 × 2048 px ²
Region of interest (ROI)	30 × 30 mm ²
Tracer molecule	Acetone gas
Emission wavelength	405 nm
Number of pairs	300 pairs (integration of 10 shots for each image)

Table 3. The MTV system parameters.

3.4. Measurement uncertainty analysis

Measurement uncertainty is an inherent aspect of any experimental technique, requiring a comprehensive analysis of its sources to ensure reliable results. In this study, the Guide to the Expression of Uncertainty in Measurement (GUM) framework (ISO, OIML & BIPM 2009) was utilised to calculate standard uncertainty by identifying influencing factors, evaluating Type A (random) and Type B (bias) uncertainties, and determining the combined standard uncertainty. Consideration of the correlation between elements and their respective sensitivity coefficients was essential, using the root sum of squares method for independent elements. Finally, the extended uncertainty is obtained by multiplying the combined uncertainty by an appropriate coverage factor (k) to account for the level of confidence.

3.4.1. The PIV uncertainty analysis

The ability of tracer particles to follow the flow in PIV applications, particularly in supersonic free jets, is typically verified using the Stokes number. Traditionally, the Stokes number is calculated at the nozzle outlet, which serves as a reference point for flow characterisation because it typically exhibits the highest velocity in incompressible free jets, and the highest Stokes number (which presents the worst condition for particle tracking). However, in compressible flows such as supersonic free jets, the flow velocity increases further beyond the nozzle outlet in the transient expansion region, particularly before the Mach disk in the first shock cell. This highlights the need for more nuanced approaches when analysing compressible flows under rarefied conditions. In this study, the Stokes number is calculated at the nozzle outlet, similar to previous studies in supersonic free jets (De Gregorio 2014; Edgington-Mitchell *et al.* 2014b). However, we further investigated the downstream evolution of the Stokes number, particularly within the zone of silence, where rapid density decreases significantly affect particle traceability (refer to Appendix C).

Measurement uncertainty in PIV, which has been extensively studied in previous research (Sciacchitano & Wieneke 2016; Sciacchitano 2019), depends on the magnification factor M , time interval Δt , and pixel displacement Δs , which determine the velocity of tracer particles. It is critical that particles adequately follow the flow, a condition assumed if the corrected Stokes number is significantly less than unity. Before calculating these uncertainties, image distortion was carefully addressed to ensure accuracy in the measurements. Perspective error, which can arise from optical distortion caused by wide-angle lenses, was minimised by using a small ROI and verifying alignment with a reference object placed in the light sheet plane. Particle image sizes were compared between the centre and edges of the frame to confirm the absence of significant distortion, and depth of

field checks ensured that all particles within the laser sheet were in focus. Additionally, the vacuum chamber was translated during set-up to maintain optical alignment. Once image distortion was confirmed to be negligible, the standard uncertainty of the magnification factor is measured by the pixel resolution, using a triangular probability distribution based on the maximum and minimum values of the image of a ruler placed in the light sheet plane prior to the PIV measurements. Similarly, the standard uncertainty of the time interval is derived from the temporal resolution of the timing hub, as specified by the manufacturer, employing a rectangular probability distribution. The standard uncertainty of pixel displacement was set at 0.1 pixel, made feasible by the use of nano-particle-based Rayleigh scattering. These uncertainties are combined, and a coverage factor $k \approx 2$ for 95 % level of confidence is applied to determine the extended uncertainty. In this study, specific uncertainties arising from shockwaves and Rayleigh-scattering-induced optical distortions due to steep flow property (e.g. density or temperature) gradients were not considered, as the main quantitative PIV analysis was conducted in the far-field zone where these issues are not prominent. The maximum overall uncertainty of PIV is 7.1 % in a highly under-expanded regime, with the detailed uncertainty budget presented in [table 4](#).

3.4.2. The MTV uncertainty analysis

Unlike PIV, where uncertainty sources are well documented, MTV uncertainty remains less studied, with early applications identifying factors such as flow unsteadiness and image degradation. While consensus on estimation methods is lacking, recent efforts have advanced quantification. In this study, we applied the latest analytical methods to assess MTV uncertainty (Pitz & Danehy 2020).

In our investigation, MTV is employed in a one-dimensional fashion focusing solely on measuring streamwise velocity. Consequently, the standard uncertainty associated with factors such as magnification factor and time interval aligns with that of PIV. However, MTV has an additional source of uncertainty related to spanwise velocity assumptions, as elucidated in Mustafa *et al.* (2017). Typically, this entails assuming an uncertainty equivalent to 5 % of the freestream velocity. For our analysis, we assume the velocity beyond the main jet to represent the freestream velocity. The uncertainty in streamwise pixel displacement was determined based on previous studies (Gendrich & Koochesfahani 1996; Ramsey & Pitz 2011). The accuracy of determining streamwise pixel displacements relies on precise Gaussian fitting, assessed quantitatively through the SNR, defined as

$$\text{SNR} = \frac{S_p}{4\sigma_N}, \quad (3.1)$$

where S_p represents the peak intensity obtained from Gaussian fitting, while σ_N signifies the standard deviation of noise, which comes from the residual values after the Gaussian fit is subtracted from the experimental data. Through the SNR, the accuracy of Gaussian fitting can be assessed, facilitating the quantification of uncertainty in pixel displacement. When the SNR exceeds 4, the uncertainty in pixel displacement is typically approximately 0.2 pixel considering the laser linewidth. For instance, as depicted in [figure 7\(a\)](#), the first image exhibits a high SNR at 11.6, indicating precise peak identification. Conversely, in subsequent shots such as the delayed second image, both emission intensity and SNR decrease. However, despite the decrement, the peaks still exhibit sufficient reliability, as shown in [figure 7\(b\)](#). On the contrary, in cases such as [figure 7\(c\)](#) with a lower SNR, the uncertainty in pixel displacement increases significantly, rendering the data unsuitable for velocity calculation. Such data were excluded from our analysis, with

Source of uncertainty	Exp. value (unit) -10 torr-	Standard uncertainty	Probability distribution	Divisor	Degrees of freedom
M	$21.0 \mu\text{m pixel}^{-1}$	$u_M = \frac{\text{pixel resolution}}{\sqrt{6}}$	Triangular	0.41	∞
Δt	Min, 264 ns; Max, 2250 ns	$u_{\Delta t} = \frac{\text{temporal resolution}}{2\sqrt{3}}$	Rectangular	0.29	∞
Δs	Min, 3.65 pixel; Max, 5.97 pixel	$u_{\Delta s} = 0.1 \text{ pixel}$	–	–	∞
Extended relative uncertainty (95 % level of confidence)	$2\sqrt{\frac{u_M^2}{M^2} + \frac{u_{\Delta t}^2}{\Delta t^2} + \frac{u_{\Delta s}^2}{(\text{mean}(\Delta s))^2}}$			10 torr, 7.1 % (maximum)	

Table 4. The PIV uncertainty budget.

Notes: The PIV uncertainty at 1 torr was omitted due to inconsistencies in both near-field and far-field zones.

Source of uncertainty	Exp. value (unit) -10 torr-	Exp. value (unit) -1 torr-	Standard uncertainty	Probability distribution	Divisor	Degrees of freedom
M	18.9 $\mu\text{m pixel}^{-1}$	18.9 $\mu\text{m pixel}^{-1}$	$u_M = \frac{\text{Pixel resolution}}{\sqrt{6}}$	Triangular	0.41	∞
Δt	200 ns	Min, 300 ns; Max, 750 ns	$u_{\Delta t} = \frac{\text{Temporal resolution}}{2\sqrt{3}}$	Rectangular	0.29	∞
Δx	3.2 pixel	Min, 5 pixel; Max, 10 pixel	$u_{\Delta x} = 0.2 \text{ pixel}$	–	–	∞
Δy	(*)	(*)	$u_{\Delta y} = 5\% \text{ of freestream velocity}$	–	–	∞
Extended relative uncertainty (95 % level of confidence)	$2\sqrt{\frac{u_M^2}{M^2} + \frac{u_{\Delta t}^2}{\Delta t^2} + \frac{u_{\Delta x}^2}{(\text{mean}(\Delta x))^2} + \frac{v_{y,rms}^2}{v_x^2} \left(\frac{dv_x}{dy}\right)^2 \Delta t^2}$				10 torr, 6.71 %(maximum); 1 torr, 8.33 %(maximum)	

Table 5. The MTV uncertainty budget.

(*) Standard uncertainty of $u_{\Delta y}$ was accounted for at different locations when calculating the combined uncertainty, yielding the maximum value.

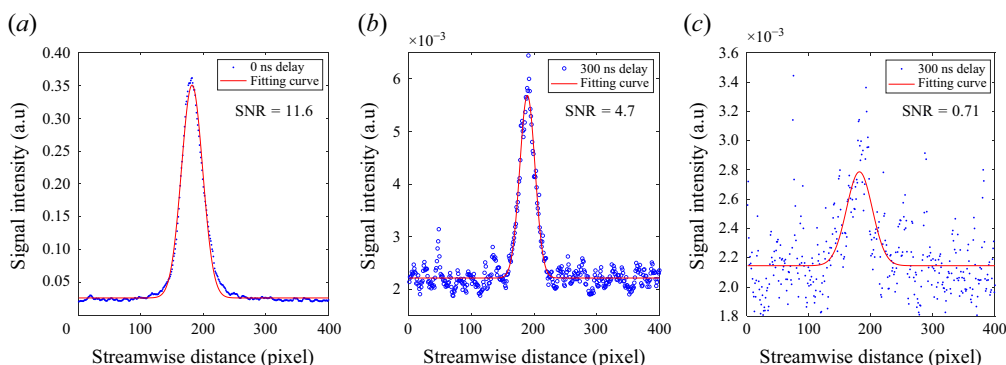


Figure 7. Signal intensity of (a) first image, (b) second image with Gaussian fitting for high SNR, and (c) second image with Gaussian fitting at low SNR.

calculations performed only on Gaussian fits with SNR exceeding 4. The maximum overall uncertainties of MTV are 6.71 % in a highly under-expanded regime, and 8.33 % in an extremely under-expanded regime, as detailed in [table 5](#).

4. Results and discussion

4.1. Highly under-expanded supersonic free jet (turbulent flow regime)

4.1.1. Shockwave structure

The LIF was performed to visualise the shockwave structure of the supersonic free jet under the conditions listed in [table 1](#). The LIF image shown in [figure 8\(a\)](#) was obtained by ensemble averaging 100 individual images using an integration technique. This approach averages out fluctuations and highlights the overall flow characteristics. [Figure 8\(a\)](#) illustrates the presence of oblique shocks and a Mach disk at the outlet, along with a cyclical wake structure that shows a highly under-expanded regime within the supersonic free jet. This visualisation closely resembles observations of shockwave structures in supersonic free jets at atmospheric pressure, as depicted in [figure 8\(b\)](#).

4.1.2. Near-field zone

In a jet, velocity remains constant in the potential core before decaying in the fully developed region, forming a Gaussian profile. Consequently, centreline velocity is commonly used to assess jet behaviour. However, in supersonic jets, oblique and normal shockwaves disrupt this pattern, preventing a uniform or Gaussian profile. The normal shockwave notably reduces velocity, making the centreline velocity lower than the surrounding flow. Therefore, in supersonic jets, both centreline and maximum velocities were evaluated to capture the jet's overall characteristics. [Figure 9](#) presents the axial variation of the centreline and maximum streamwise velocity, where the axial distance has been normalised by the nozzle diameter. Similarly [figure 10](#) presents the radial variation of streamwise velocity at selected axial locations. Again, the radial distance has been normalised by the nozzle diameter. Notably, there are substantial disparities between PIV and MTV measurements in the near-field zone. Initial variations between MTV and PIV likely stem from the influence of free expansion and shockwaves, while measurements downstream show converging values.

[Figure 9](#) suggests that in the near-field zone, PIV tracer particles generally fail to follow the flow accurately. After exiting at Mach 1 ($\sim 320 \text{ m s}^{-1}$) from the sonic nozzle, the velocity increases as it passes through the first expansion zone, which is a continuum

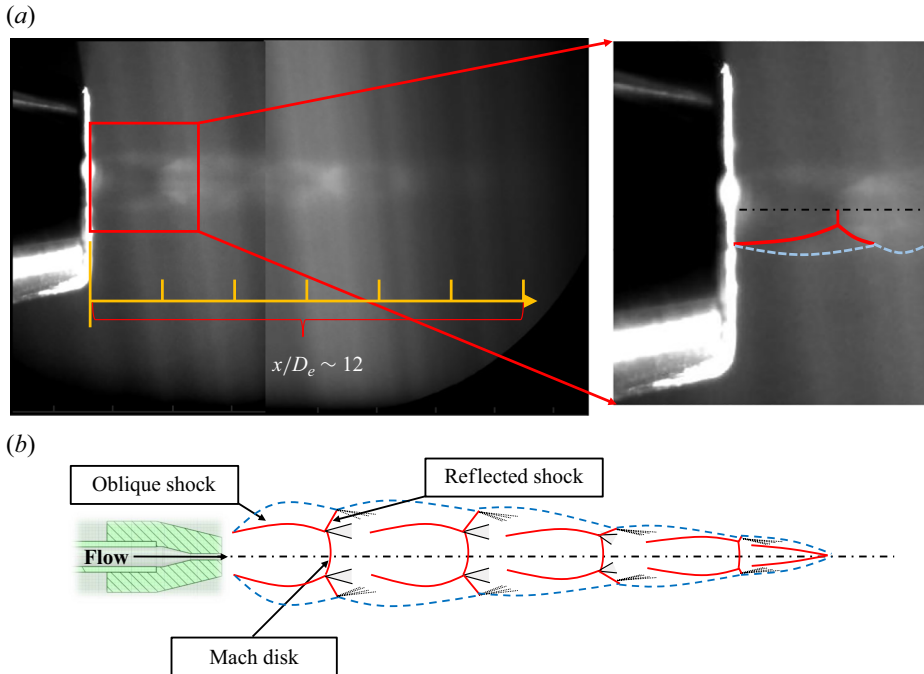


Figure 8. Combined LIF field of view for highly under-expanded supersonic free jet: (a) cyclical shockwave structure in the near-field zone where the axial distance has been normalised by the nozzle diameter (D_e), and (b) schematic of flow structure.

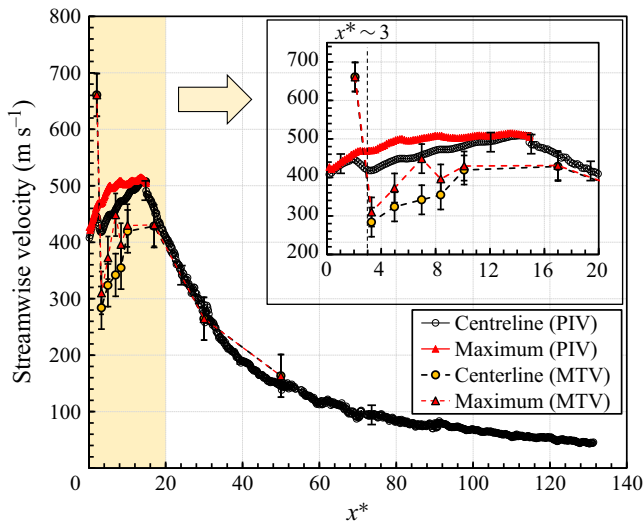


Figure 9. Evolution of centreline and maximum streamwise mean velocities from PIV and MTV.

region without shockwaves (figure 1). The PIV shows an initial increase in velocity in this expansion zone, but MTV cannot do so due to laser sheet thickness limits, leading to light reflections from the nozzle that introduce noise and obscure measurements, especially in highly under-expanded supersonic jets with small shockwave structures. Both results suddenly decrease at $x/D_e \sim 3$ after the Mach disk. The reduction in velocity is

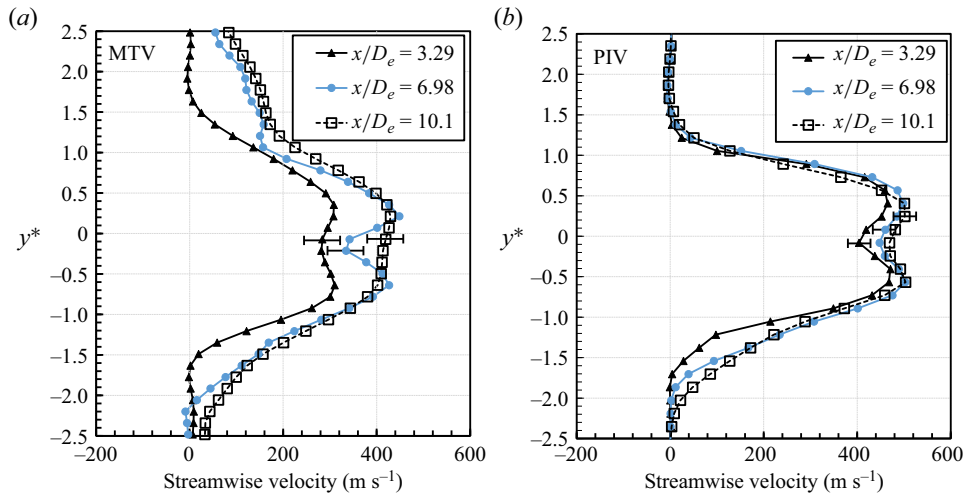


Figure 10. Streamwise mean velocity profile in the near-field zone for (a) MTV and (b) PIV.

significantly more pronounced in MTV than in PIV. After this decrease, PIV shows a slight steady increase, while MTV shows a stronger increase. This discrepancy suggests that PIV particles may not effectively follow the rapid changes in velocity and flow gradients through the shockwave zone. Additionally, Rayleigh scattering effects, particularly in regions of large temperature and density gradients, may influence the PIV measurements.

To observe more detailed velocity changes, we compared streamwise mean velocities from MTV and PIV at various positions in the near-field zone after the Mach disk (figure 10). Both experiments show similar profile shapes, but MTV reports significantly lower velocities, especially at $x/D_e = 3.29$. This difference is due to the velocity reduction after the shockwave which the PIV tracer particles cannot sufficiently resolve. Furthermore, instead of a Gaussian distribution jet profile, a dual-peak velocity profile exists, due to influence from the Mach disk. The Mach disk is generally considered a normal shockwave with low pressure difference. However, when there is a significant pressure difference, curvature occurs, causing only the central part to behave as a normal shockwave, while the surrounding areas experience a weaker shock. This results in significant velocity reduction at the centre, with less reduction in the surrounding regions, leading to a dual-peak velocity profile. Both MTV and PIV show an increase in velocity downstream after the Mach disk, with velocities in the centre region increasing due to the favourable pressure gradient.

Velocity profiles are overlaid in figure 11(a) to compare the velocity reduction near the jet exit. Initially, MTV velocities are faster, but after the Mach disk, the centreline velocity decreases by more than half, while PIV shows only a slight reduction. This suggests that in a rarefied environment, the discrete changes in fluid properties, such as pressure and density caused by the shockwave, lead to a rapid increase in the Stokes number. The particle relaxation time scale increases more relative to the increase in the fluid time scale, thus the particles are not able to suddenly reduce their velocity, which is the case shown by MTV. A direct comparison of post Mach disk velocity profiles is similarly overlaid in figure 11(b). As the streamwise mean velocity profile indicates, the jet gradually spreads radially downstream, showing a slight velocity increase. However, the PIV does not properly capture this.

The MTV data are featured in figure 12 to examine the evolution of the entire jet velocity profile in the near-field zone. The jet velocity has a single strong peak near the outlet before

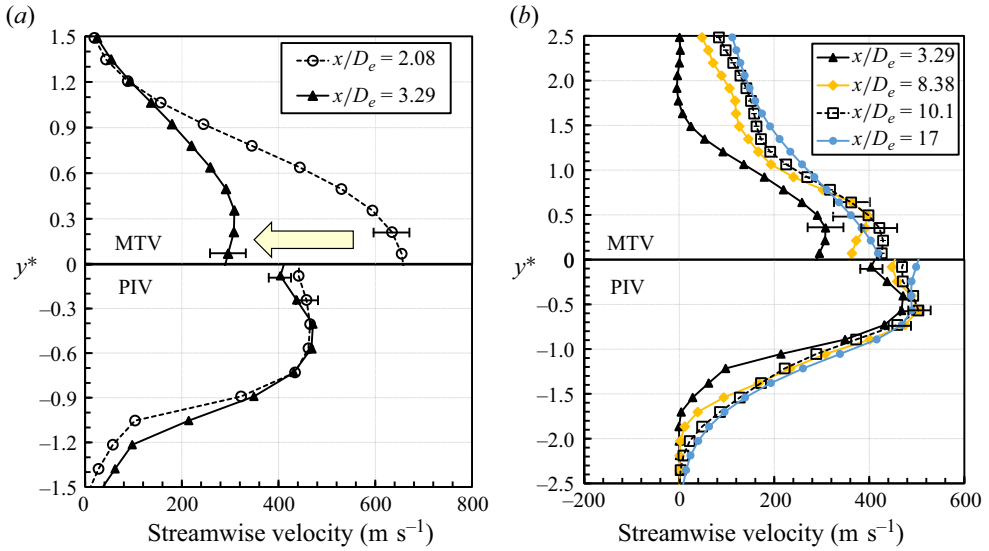


Figure 11. Streamwise mean velocity profiles (a) before and after the Mach disk and (b) comparisons after the Mach disk in the near-field zone.

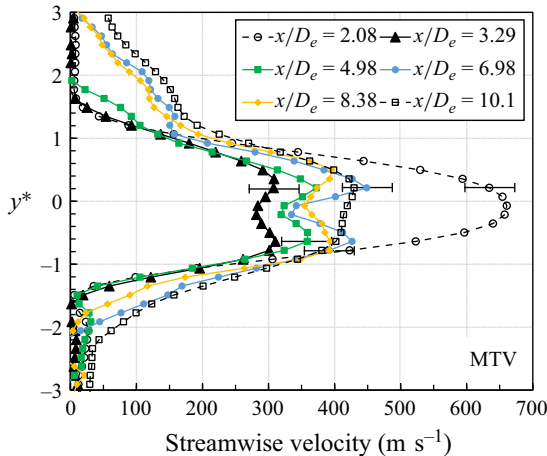


Figure 12. Evolution of the streamwise mean velocity profile in the near-field zone using MTV.

reaching the Mach disk, then substantially diminishes to form two peaks, and subsequently increases while the jet gradually spreads radially outward. The dual-peak pattern becomes most prominent at $x/D_e = 6.98$, likely due to the influence of the reflected shockwave in the surrounding area after the Mach disk. The centreline velocity continues to increase thereafter, and eventually, as the centreline and maximum velocities become similar, the dual-peak velocity profile gradually disappears.

4.1.3. Far-field zone

The velocity distribution in the far-field zone was also illustrated in figure 9. It is noteworthy that both MTV and PIV showed converging centreline and maximum velocity distributions. The alignment of the distributions suggests that in the far-field zone, the

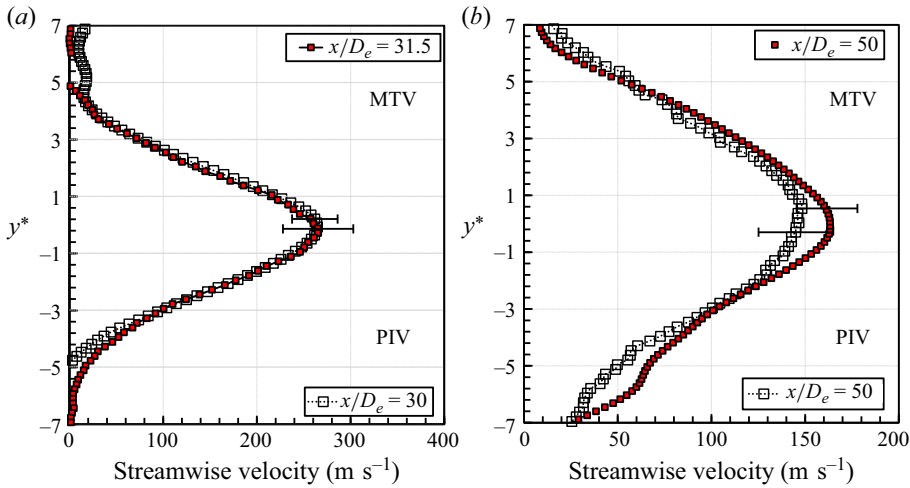


Figure 13. Streamwise mean velocity profile comparison between MTV and PIV at (a) $x/D_e = 30$ and (b) $x/D_e = 50$.

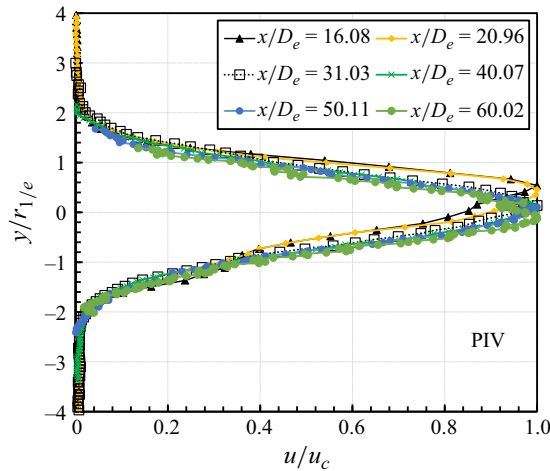


Figure 14. Streamwise mean velocity profiles (PIV) in the far-field zone normalised with centreline velocity (u_c) and jet radius ($r_{1/e}$) defined by the radial distance where the streamwise velocity decreases to $1/e$ of the centreline maximum velocity.

absence of shockwave structures allows PIV to effectively follow the flow. Figure 13 demonstrates that the MTV and PIV streamwise mean velocity profiles are similar, adhering to a Gaussian profile, without the characteristic dual peaks observed in the near-field zone. This indicates that these measurement techniques are consistent with each other in capturing the flow in the far-field zone, and suggests that the jet exhibits self-similarity akin to a subsonic free jet.

Indeed, as shown in figure 14, normalised streamwise mean velocity profiles at various streamwise locations collapse onto each other, confirming the jet's self-similarity. This also allows for calculation of the jet spreading rate, as depicted in figure 15. The observed spreading rate of approximately 0.1 is consistent with that of a turbulent jet, implying that the jet in the far-field zone is turbulent.

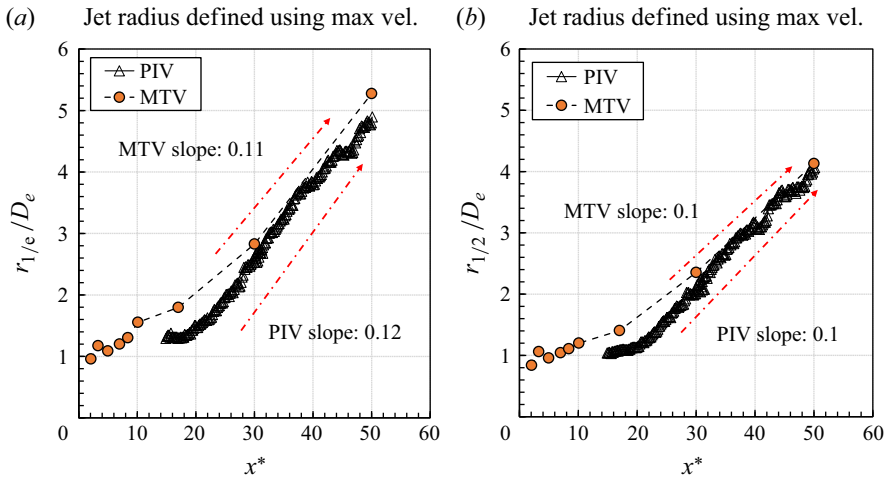


Figure 15. Normalised jet radius defined by the radial distance where the streamwise velocity decreases to (a) $1/e$ and (b) half of the maximum velocity.

As the jet satisfies self-similarity, modelling of the centreline velocity in the far-field zone can proceed in a manner similar to that of a subsonic jet. However, as noted by Birch, Hughes & Swaffield (1987), the decay constant varies with the NPR, different to typical incompressible turbulent jets. The evolution of the centreline velocity, incorporating the NPR, is displayed in figure 16. The current slope 0.193 aligns with studies conducted under atmospheric pressure conditions (Ball, Fellouah & Pollard 2012). This relationship can be expressed as

$$\frac{u_c}{V_e} = \kappa \left(\frac{x+a}{D_e} \right)^{-1} \sqrt{\frac{P_0}{P_\infty}}, \quad (4.1)$$

where u_c is the centreline velocity, V_e is the outlet velocity magnitude, κ is the decay constant, x is the streamwise position, and a is the momentum virtual origin. From the linearised form of the data in figure 16, the value of $1/\kappa$ was determined to be approximately 0.193, corresponding to a decay constant $\kappa \sim 5.18$. To determine the momentum virtual origin a , a least mean squares fitting approach was employed to maximise the R^2 value (0.99) of the fit. This yielded $a = 13.66D_e$, ensuring the highest accuracy in representing the data.

The PIV data were used to calculate turbulent statistics in the far-field zone. Figure 17 presents both centreline streamwise and spanwise turbulence intensities that increase moving downstream, peaking at approximately $x/D_e = 60-70$ before decreasing. This peak can be attributed to the delayed convergence of turbulent energy in the fully developed region. While the jet achieves self-similarity in mean velocity earlier, turbulent characteristics continue to evolve downstream. Statistics of streamwise (u') and spanwise (v') velocity fluctuations converge later compared to those of the mean velocity, causing turbulence intensity to peak at $x/D_e = 60-70$ before decreasing as the flow becomes fully turbulent. Streamwise turbulence intensity converges at approximately 28%, while spanwise turbulence intensity seems to converge at approximately 20%, aligning with results from previous studies (Wynanski & Fiedler 1969; Panchapakesan & Lumley 1993; Xu & Antonia 2002; Burattini, Antonia & Danaila 2005; Quinn 2006). These studies also demonstrated that turbulence intensity reaches a steady value in the fully developed

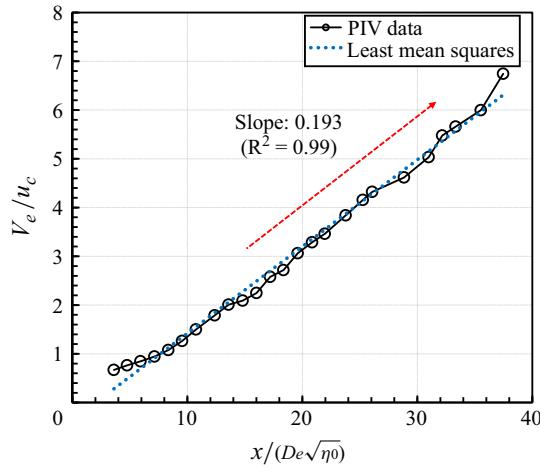


Figure 16. Evolution of inverse normalised centreline streamwise mean velocity.

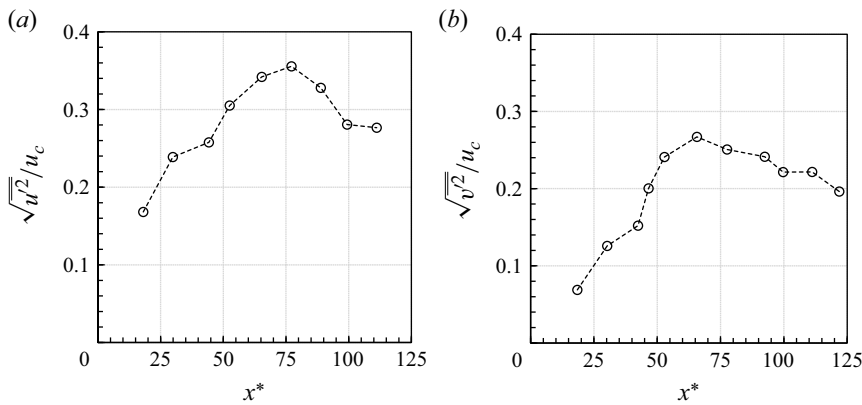


Figure 17. Evolution of centreline (a) streamwise and (b) spanwise turbulence intensity.

region of turbulent jets, reflecting self-similarity after sufficient mixing. The agreement with these studies further supports the classification of the far-field jet as being turbulent.

Normalised turbulence intensity profiles are plotted in figure 18. The streamwise turbulence intensity displays more distinctive dual-peak patterns compared to the spanwise case. Additionally, the Reynolds shear and normal stress profiles are presented in figure 19, demonstrating close similarity to Reynolds stresses of atmospheric turbulent free jets observed in previous experimental results (Hussein, Capp & George 1994). This further indicates that the turbulent viscosity, which is determined by the gradient of the streamwise mean velocity and Reynolds shear stress, also follows a similar pattern. Furthermore, proper orthogonal decomposition (POD) analysis was conducted to analyse the coherent structures of turbulence in the far-field zone. The detailed methodology and results of the POD analysis have been included in Appendix D for further reference. Overall, the results reveal that turbulent jet behaviour remains similar with atmospheric conditions. Even as the flow becomes more rarefied and stable, its characteristics are preserved under reduced pressure.

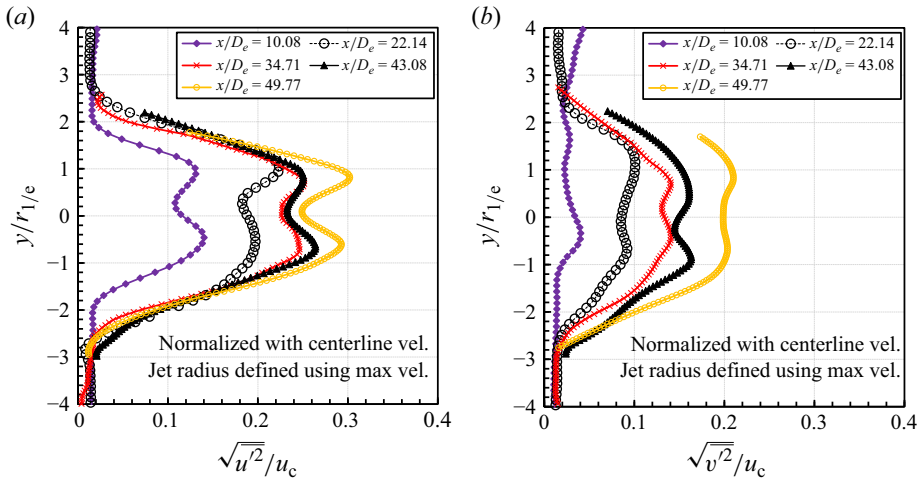


Figure 18. Turbulence intensity profiles for various downstream positions in the far-field zone.

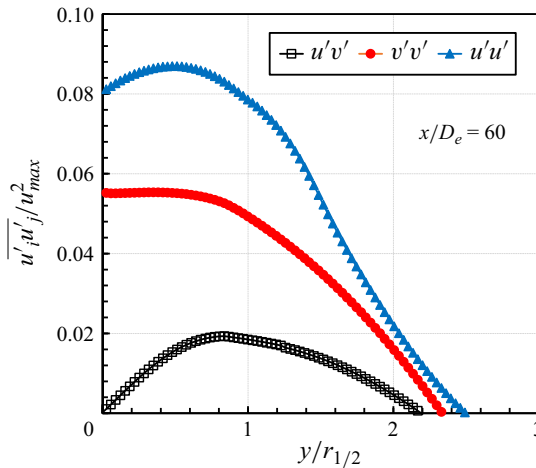


Figure 19. Reynolds stress profiles at $x/D_e = 60$ in the far-field zone.

4.2. Extremely under-expanded supersonic free jet (laminar flow regime)

4.2.1. Shockwave structure

The LIF was performed to visualise the structure of the supersonic free jet under the conditions listed in [table 1](#). The LIF image shown in [figure 20](#) was obtained by ensemble averaging 100 individual images using an integration technique. As clearly depicted in [figure 20\(a\)](#), the presence of a barrel shockwave and a central Mach disk can be identified. Beyond the Mach disk, no additional shockwave structures are observed, and a long annular shear layer persists in the far-field zone. The Mach disk exhibits slight curvature due to the high pressure difference. Studies examining shockwave structures of a supersonic free jet in a rarefied environment with NPR exceeding 100 are scarce, but comparisons with a limited number of studies reveal a very similar structure (Volchkov *et al.* 1973; Belan *et al.* 2008, 2011; Shurtz & West 2022). The key features at each location are indicated schematically in [figure 20\(b\)](#). The annular shear layer within the

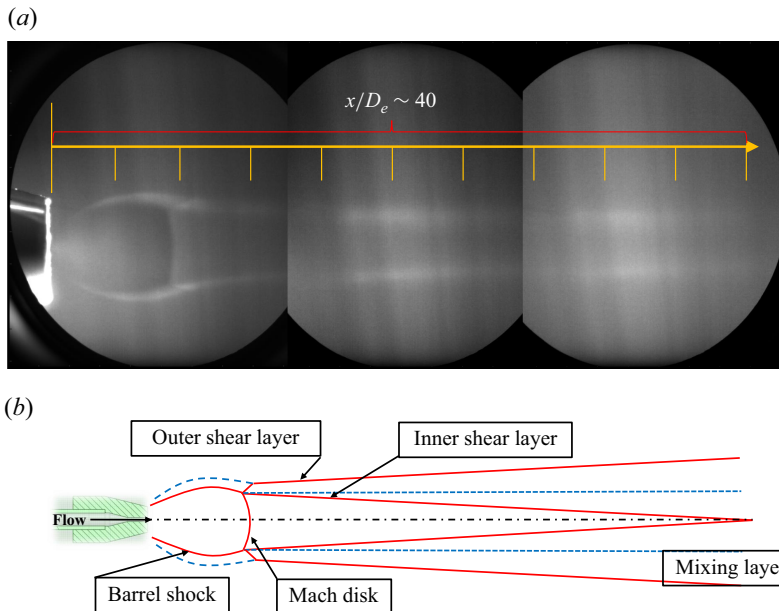


Figure 20. Combined LIF field of view for extremely under-expanded supersonic free jet: (a) single-barrel shockwave with long annular shear layer, and (b) schematic of flow structure.

inner and outer shear layers fundamentally acts as a mixing zone. The mixing stems from the dual-peak velocity profile created by the Mach disk, with shear arising between the velocity peak and both the slower-moving jet interior (inner region) and ambient fluid (outer region).

4.2.2. Near-field zone

Similar to a highly under-expanded supersonic free jet, to analyse the overall characteristics of the jet considering the shockwave structure, we assessed the centreline and maximum velocities. In the case of an extremely under-expanded supersonic free jet, as illustrated in figure 21, the initially discharged flow undergoes a sharp velocity increase due to free expansion. The differences between MTV and PIV are even more pronounced than for the previous highly under-expanded supersonic free jet. While MTV appears to track this sudden increase accurately, PIV registers only a slight velocity increase. As the gas exits the nozzle, the tracer particles are unable to respond to the flow field changes, due to the decreased surrounding density following the expansion. After the initial spike in velocity, a subsequent sharp decrease occurs due to the Mach disk at $x^* \approx 8$. Both MTV and PIV record a velocity decrease, but the reduction in PIV is significantly less pronounced compared to MTV. Mach disks increase the pressure, which then expands to match downstream conditions, resulting in an increasing velocity. The MTV captures this velocity increase due to the favourable pressure gradient. In contrast, PIV shows a prolonged decrease as the tracer particles' inertia exceeds the pressure gradient, unlike in the 10 torr case. After the jet pressure equalises with the ambient pressure, the jet reaches the fully developed region where the centreline and maximum velocities converge, as seen from both MTV and PIV results.

Given the notable difference between MTV and PIV results in the near-field zone, a comparison with theoretical values is warranted. The theoretical Mach disk position and size were calculated using the following empirical equations, derived for conditions of

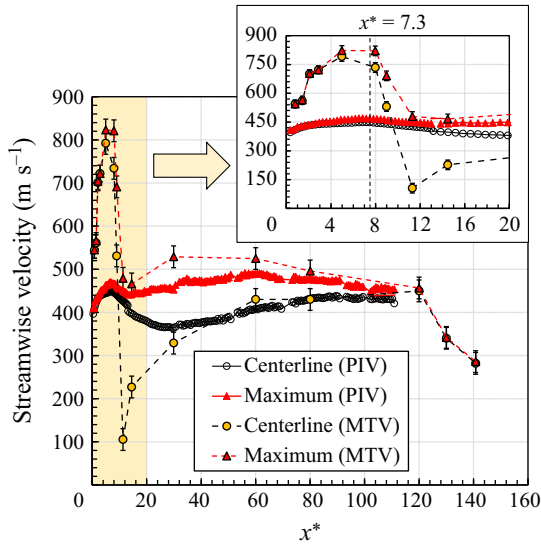


Figure 21. Evolution of centreline and maximum streamwise mean velocities for PIV and MTV.

ambient pressure higher than atmospheric pressure (Lewis, Clarke & Carlson 1964; Crist, Glass & Sherman 1966; Jiang *et al.* 2022):

$$\frac{L_{Mach}}{D_e} = 0.64\eta_0^{0.5}, \quad (4.2)$$

$$\frac{D_{Mach}}{D_e} = 0.37\eta_0^{0.5}, \quad (4.3)$$

where L_{Mach} and D_{Mach} are the position and diameter of the Mach disk, respectively. The normalised positions of the Mach disk calculated using the equations are 7.3 for its normalised location, and 3.2 for its normalised diameter. We also determined the position of the Mach disk from the experimental data. Both the MTV centreline and maximum velocity results show a sharp decrease after normalised position 7.98, thus this was deemed to be the location of the Mach disk. This closely matches the Mach disk position observed in LIF measurements, with slight discrepancies attributed to the MTV spatial resolution limits. The results also align well with established empirical equations.

Next, we compare the flow properties at the zone of silence. Functional dependence of the Mach number $M(x)$ on downstream distance x can be determined using the following equation (Morse 1996) for a jet exiting from a sonic nozzle:

$$M(x) = A \left(\frac{x - x_0}{D_e} \right)^{\gamma-1} - \frac{(\gamma + 1)/(\gamma - 1)}{2A[(x - x_0)/D_e]^{\gamma-1}}, \quad (4.4)$$

where γ is the specific heat ratio, and x_0/D_e and A depend on γ . The parameter A is a coefficient introduced by Morse (1996) that depends on the nozzle geometry and characterises the specific expansion properties of the jet. For a supersonic free N_2 jet, γ is 1.3, resulting in $x_0/D_e = 0.7$ and $A = 3$. It is important to note that (4.4) is not influenced by the NPR or the Reynolds number. Instead, it was derived analytically based on the free expansion of fluid from a sonic nozzle, and describes the centreline Mach number development within the zone of silence, a region of adiabatic, non-viscous expansion. As discussed in Rebrov (2001), this equation assumes that the zone of silence remains in the continuum regime, surrounded by the barrel shock up to the Mach disk, where isentropic

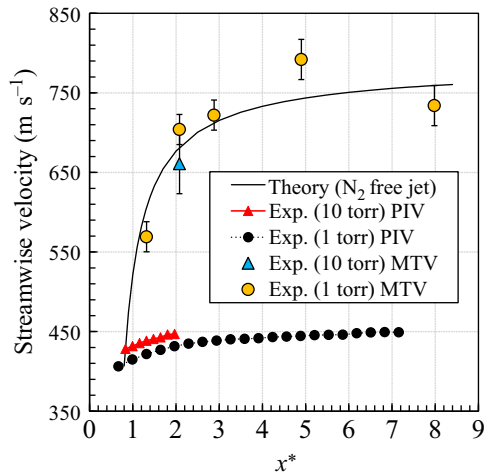


Figure 22. Comparison between experimental centreline streamwise velocity and theory.

relations apply. If the flow at the nozzle outlet were not in the continuum regime, then (4.4) would no longer be valid. However, in our study, the flow at the nozzle outlet meets this criterion, allowing us to apply this model.

Using the aforementioned equation and isentropic relation, absolute streamwise velocity can be determined and compared with experimental results. Figure 22 presents comparisons among theoretical, MTV and PIV results for centreline streamwise velocity. The zone of silence up to the Mach disk is a free expansion zone and should exhibit the same velocity profile for both ambient pressures. As is evident from the plot, PIV data do not align with theoretical values, regardless of the pressure condition (1 torr or 10 torr). Additionally, theoretical streamwise velocity before and after the Mach disk was calculated using Mach numbers derived from the calorically perfect normal shock relation. From these calculations, the theoretical velocity was estimated to be approximately 126 m s^{-1} . This value corresponds to the lowest streamwise velocity observed in the post-Mach-disk region, and aligns closely with the MTV measurement 105 m s^{-1} , considering experimental uncertainties as depicted in figure 21.

To observe the evolution of the streamwise mean profile in the near-field zone, velocity profiles at various streamwise positions before and after the Mach disk are presented for the MTV results in figure 23. Figure 23(a) illustrates that the velocity consistently increases after the jet is discharged from the nozzle due to flow expansion. In figure 23(b), the velocity profile is deformed due to interactions with the barrel shock, and decreases (as expected) after the Mach disk, forming a distinct double-peak profile. As the jet progresses downstream, velocities gradually increase, primarily due to favourable pressure gradients. This velocity increment phenomenon for a one-barrel shock is similarly observed in supersonic free jets at atmospheric pressure (Jerónimo *et al.* 2002; Xiao *et al.* 2019).

In a supersonic free jet, the potential core extends to the point where the annular shear layers merge at the jet centreline (Franquet *et al.* 2015). In our study, this zone is identified as the point where the centreline and maximum velocities become equal to each other, as illustrated in figure 21. The primary focus within this zone is the development of the mixing layer, particularly how the inner and outer shear layers evolve due to the influence of the Mach disk. Unlike the zone of silence, this region is significantly affected by viscosity, making the application of isentropic relations challenging.

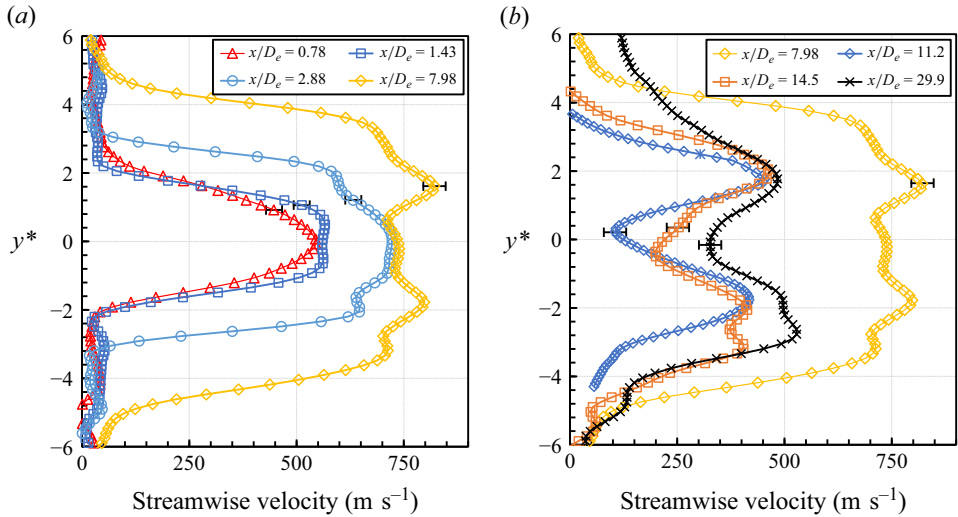


Figure 23. Streamwise mean velocity profiles (a) before and (b) after the Mach disk.

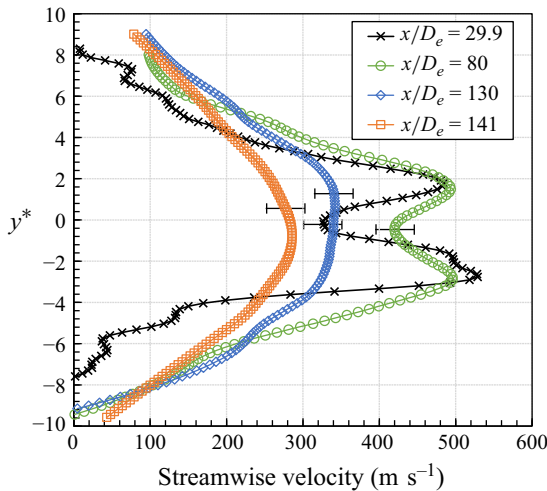


Figure 24. Evolution of streamwise mean velocity profile in the potential core region and far-field zone.

Further analysis was conducted by examining the streamwise mean velocity profiles obtained from MTV at key locations after the Mach disk at $x/D_e = 7.98$, as presented in [figure 24](#). Following the Mach disk, the velocity profile exhibits a large dual peak with a substantial velocity gradient. As the flow progresses downstream, both inner and outer shear layers develop concurrently. Eventually, these dual peaks merge into a single peak as the flow transitions into the far-field zone in [figure 21](#). Subsequently, as the momentum diffuses outwards, the centreline velocity begins to decay, and the jet spreads radially outward.

4.2.3. Far-field zone

The velocity distribution in the far-field zone was also illustrated in [figure 21](#). A dramatic velocity decrease is observed. This phenomenon is attributed to two factors. First, this

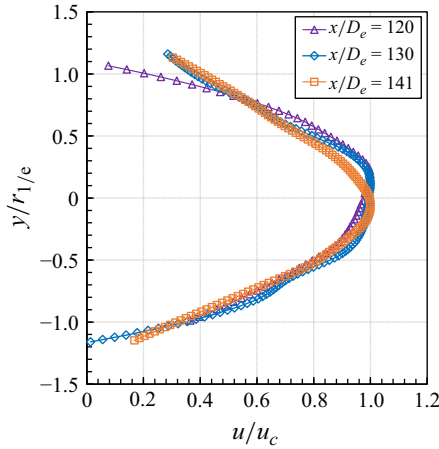


Figure 25. Self-similarity of the normalised streamwise mean velocity profile in the far-field zone.

region marks the transition from the potential core to the fully developed region. In the potential core, the centreline velocity remains high due to favourable pressure gradients and momentum transfer from surrounding high-velocity regions. In the fully developed region, the velocity profile evolves into a Gaussian distribution, leading to significant momentum transfer from the centreline to the surroundings, and a more rapid velocity decay. Second, the velocity decay in the fully developed region is proportional to the inverse streamwise distance ($1/x^*$), consistent with the behaviour of free jets observed in prior studies, such as Birch *et al.* (1987).

In the far-field zone, the jet transitions to a Gaussian-shaped fully developed velocity profile. Velocity profiles normalised by the jet radius are presented in figure 25, confirming self-similarity. The corresponding jet spreading rate is determined from shear layer development, via the MTV and PIV results in figure 26. Notably, the PIV results, owing to limitations in accurately measuring maximum velocity, do not allow for a precise assessment of jet radius. As evidenced by the MTV experimental data, the jet spreading rate remains constant at 0.03 after the Mach disk, in both the potential core and far-field zones. This is different to the expected turbulent free jet spreading rate 0.1. Note that the jet transitions from a turbulent to a laminar flow regime as it becomes rarefied (Volchkov *et al.* 1973). The spreading rate 0.03 observed in this study indicates a laminar flow regime, as it deviates from the universal spreading rate of a turbulent jet. Laminar free jets typically have a spreading rate inversely proportional to the Reynolds number, known to follow $12/Re$ (where jet radius is based on the $1/e$ velocity reduction criterion), as noted in previous studies by Rankin *et al.* (1983) and Kashi, Weinberg & Haustein (2018). Using the complex Reynolds number $Re_L = 400$ rather than the Reynolds number yields an expected spreading rate $12/Re_L = 0.03$, which is consistent with the experimental results. This provides direct evidence that the jet is laminar from the potential core region to the fully developed region.

With self-similarity established in the rarefied free jet, modelling of the centreline velocity in the far-field zone becomes feasible. An incompressible laminar jet can be described by the theoretical equation (Kashi *et al.* 2018)

$$u_c(x) = u_c(0) + (0.34 - u_c(0)) \left\{ 1 - \exp \left[-\frac{12(x - L_{pc})}{D_e Re_D} \right] \right\}, \quad (4.5)$$

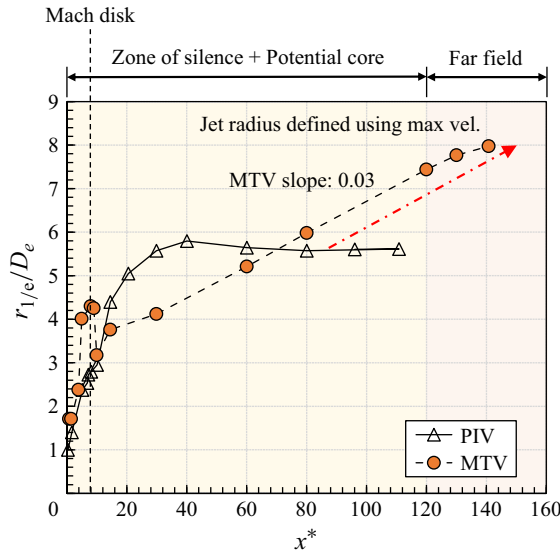


Figure 26. Normalised jet radius defined by the radial distance where the streamwise velocity decreases to $1/e$ of the maximum velocity.

where $u_c(0)$ is outlet centreline streamwise velocity normalised by outlet mean velocity (V_e), x is downstream distance, L_{pc} is the potential core length, and Re_D is the Reynolds number based on the nozzle diameter. In this study, $u_c(0)$ is assigned value 2, as the focus is on the fully developed region.

To establish the characteristic velocity, an analogy was drawn from methodologies employed in the analysis of supersonic turbulent jets, wherein the distinction between total and ambient density is represented as the NPR. The characteristic diameter D_{ch} is first defined as

$$D_{ch} = D_e \sqrt{\eta_0}. \tag{4.6}$$

As per Morton (1967), the complex Reynolds number, which determines the flow regime of the jet, remains constant regardless of the jet region, enabling us to write

$$Re_L = \frac{\rho_e V_e D_e}{\mu_e \sqrt{\eta_0}} = \frac{\rho_\infty V_{ch} D_{ch}}{\mu_\infty}, \tag{4.7}$$

where ρ_e is the exit density, V_e is the exit velocity, μ_e is the exit dynamic viscosity, ρ_∞ is the ambient density, V_{ch} is the characteristic velocity, and μ_∞ is the ambient dynamic viscosity. Rearranging this equation for characteristic velocity gives $V_{ch} = 211 \text{ m s}^{-1}$, which is used in (4.5) as the outlet mean velocity. As depicted in figure 27, there is good collapse between the experimental results and theoretical values. Notably, while (4.5) is derived for an incompressible laminar jet, it is applicable to the fully developed region of the jet in this study due to the transition to incompressible behaviour. In earlier regions, such as before the Mach disk and within the potential core, the jet exhibits compressible behaviour due to significant density and velocity variations. In contrast, in the fully developed region, the jet gradually stabilises in density and temperature as it equilibrates with the surrounding environment. Consequently, the flow behaves as an incompressible jet, allowing (4.5) to be an appropriate model for this region. Although velocity-induced compressibility effects could persist, the data suggest that such effects are negligible in the fully developed region and do not influence the flow behaviour.

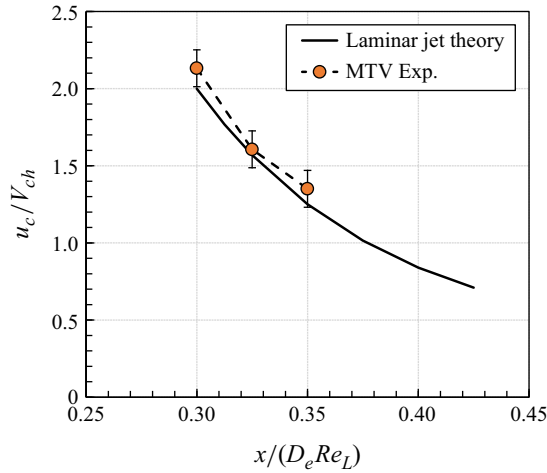


Figure 27. Evolution of normalised centreline streamwise mean velocity in the far-field zone at 1 torr.

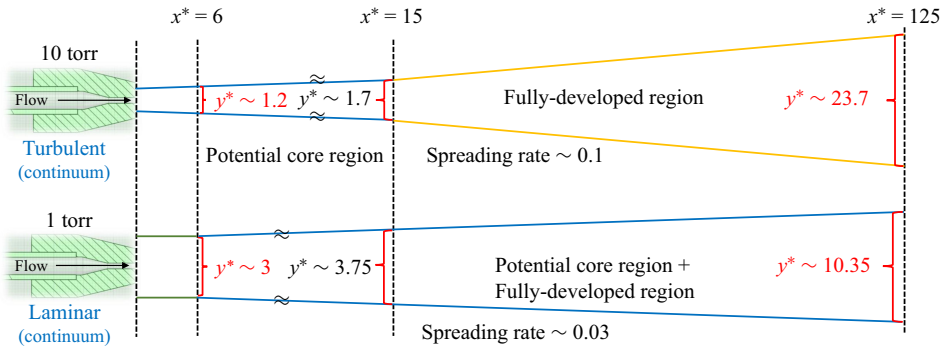


Figure 28. Overall flow structure of supersonic free jets.

In summary, this study presents experimental investigations and analyses of free jets across different flow regimes, specifically focusing on supersonic turbulent and supersonic laminar flows. Figure 28 presents a summary schematic of supersonic free jets to facilitate understanding of the experimental findings. Examination of the overall flow structure reveals distinct jet behaviours corresponding to different flow regimes. Notably, as the ambient environment becomes increasingly rarefied, the flow tends to stabilise gradually, transitioning from turbulent to laminar flow. Furthermore, it is observed that the degree of expansion upon flow exit from the sonic nozzle increases with rarefaction. At a distance $x^* = 6$ near the nozzle, it is noted that the jet radius is larger for the 1 torr free jet.

As the turbulent jet progresses downstream, it reaches the fully developed region after a short potential core, resulting in a rapid increase in jet profile, with spreading rate 0.1. Conversely, the laminar jet exhibits a lower spreading rate 0.03 for both the potential core and fully developed regions. These factors cause a difference in jet radius, with the laminar jet exhibiting a larger radius in the zone of silence due to the high NPR, while the turbulent jet radius becomes larger in the far-field zone due to its higher spreading rate (~ 0.1) compared to the laminar jet. This trend is particularly evident at $x^* = 6, 15$ and 125 . Thus the structure of supersonic free jets undergoes different variations depending on the flow regime.

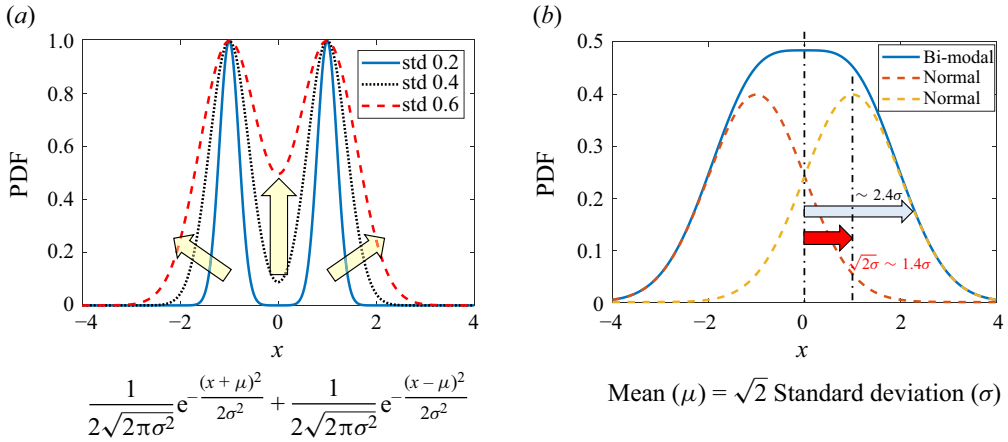


Figure 29. The probability density function (PDF) of the bi-modal distribution: (a) according to standard deviation (std), and (b) convergence into a Gaussian distribution.

4.2.4. Theoretical modelling

Jets with a long potential core region are relatively rare, resulting in limited research on modelling their velocity profiles. This study seeks to bridge this gap by analysing how velocity distributions develop beyond the potential core, and proposing a suitable modelling approach. When the NPR is moderate, the potential core region remains short, and beyond this point, the jet velocity profile typically follows a Gaussian distribution due to momentum transfer from the central region through the shear layer. However, in cases with a long potential core region, this distribution modelling becomes inaccurate due to the velocity deceleration across the diameter of the Mach disk. Utilising a bi-modal distribution allows for the effective emulation of the velocity profile, representing both the potential core and fully developed regions. As the standard deviation increases, as shown in figure 29(a), modelling captures the inner and outer shear layers. Beyond a threshold, the two distributions merge into a single Gaussian, representing the fully developed velocity profile, as illustrated in figure 29(b).

A regression can be conducted to fit the experimental data to the bi-modal distribution according to the equation

$$v_{reg} = a \exp \left[-\frac{(y/D_e + b)^2}{c^2} \right] + a \exp \left[-\frac{(y/D_e - b)^2}{c^2} \right] + d, \quad (4.8)$$

where v_{reg} is the regression result of the velocity for a bi-modal distribution centred at 0. The constant a represents the maximum value of the peak, b represents the symmetry origin, and c represents the radius of each jet. A velocity offset d was introduced to improve the fit, ensuring that d never exceeds 10% of the maximum value of v_{reg} . This expression matches the MTV results well, within the measurement uncertainty.

To assess whether the bi-modal distribution effectively models both the potential core and fully developed regions, comparisons were made with MTV experimental results at 1 torr. Figure 30 compares the derived bi-modal distribution with the corresponding experimental data for six locations. As is evident from the regression, the bi-modal distribution effectively models the inner and outer shear layers in the potential core region, while in the fully developed region, the two velocity peaks merge into a Gaussian distribution. This strong fit indicates that the outer and inner shear layers develop through

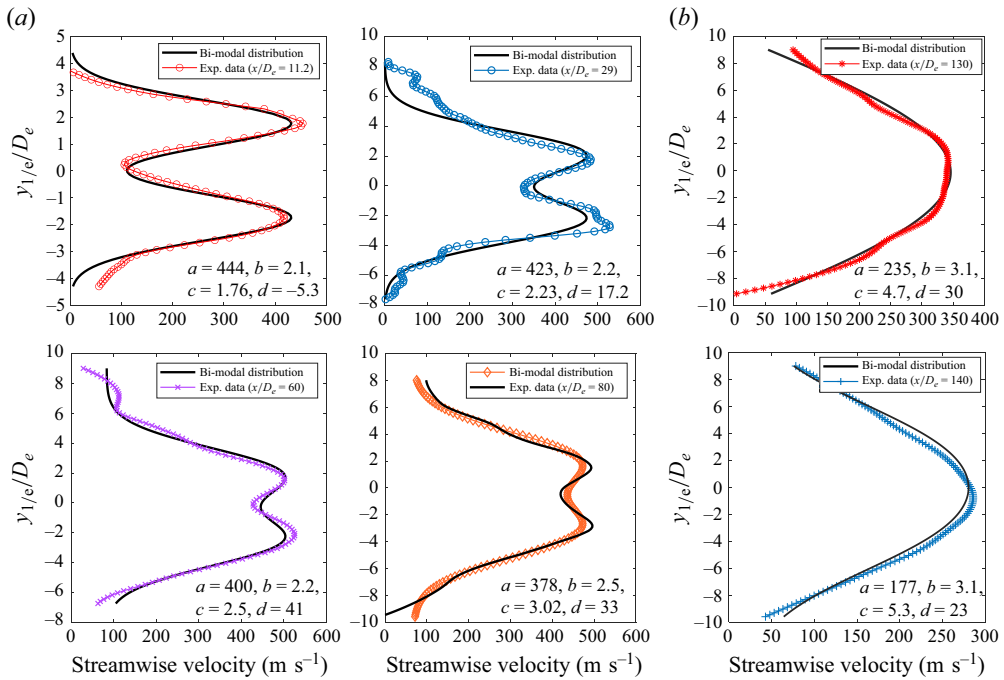


Figure 30. Streamwise mean velocity profiles from the MTV experiments and regression result of bi-modal distribution for (a) the potential core region, and (b) the far-field zone.

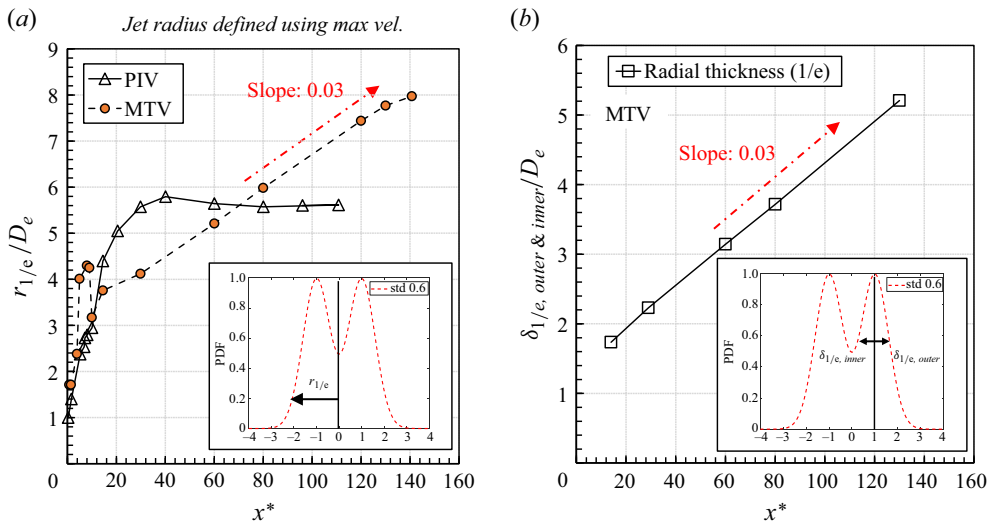


Figure 31. Normalised (a) overall jet radius and (b) inner and outer shear layer radial thickness.

momentum transfer, a mechanism similar to jet evolution in the fully developed region, reinforcing the validity of the model.

Further analysis involved verifying the development of the jet radius. In figure 31(a), the radius of the entire jet profile was determined based on the $1/e$ criterion of the maximum velocity. In figure 31(b), the radial thickness of the inner and outer shear layers

was determined based on the distance from the peak centre in the jet profile. Both radial thicknesses were found to develop at rate 0.03, indicating symmetric development of both the inner and outer shear layers, and also implying that the flow regime was laminar. These results suggest that the bi-modal distribution is adequate in representing the jet profile after the Mach disk.

By observing that both the inner and outer shear layers grow similarly to the overall jet profile following a bi-modal distribution, it becomes possible to estimate the length of the potential core region. Empirical correlations exist for determining the position and size of the Mach disk experimentally ((4.2) and (4.3)). The distance between the dual peaks of the bi-modal distribution is equivalent to the Mach disk size, as confirmed by MTV experimental data (refer to Appendix E). Additionally, the inner shear layer develops downstream following the laminar jet spreading rate. For the bi-modal distribution to transition to a Gaussian distribution, the inner shear layer must develop a distance $\sqrt{2}$ times half of the Mach disk size, as depicted in figure 29(b). Utilising this information and the definition of the spreading rate, it is possible to determine how much development length is required for the bi-modal distribution to transition to a Gaussian distribution, using the equation

$$\frac{12}{Re_L} = \frac{0.37\sqrt{2}D_e\eta_0^{0.5}/2}{\text{potential core length (PCL)} - \text{distance of Mach disk (DMD) from nozzle exit}} \quad (4.9)$$

Rearranging (4.9) for PCL, and normalising by nozzle diameter, gives

$$PCL_{lam}^* = \frac{DMD}{D_e} + \frac{0.37\sqrt{2}Re_L\eta_0^{0.5}}{24} = 0.64\eta_0^{0.5} + 0.022Re_L\eta_0^{0.5}. \quad (4.10)$$

This equation is applicable within the laminar flow regime where the complex Reynolds number ranges from 100 to 1000, and is limited to extremely under-expanded supersonic jets with a single barrel shock. Similarly, for turbulent jets under the same conditions, where $Re_L > O(10^4)$ and spreading rate 0.1 is assumed, the equation is modified by replacing $12/Re_L$ in (4.9) with 0.1, yielding the result

$$PCL_{turb}^* = 0.64\eta_0^{0.5} + 1.85\sqrt{2}\eta_0^{0.5}. \quad (4.11)$$

These newly developed correlations are first validated against experimental data across turbulent, laminar and rarefied flow regimes, demonstrating an accuracy within 10%. While errors slightly increased in the rarefied regime, likely due to Mach disk thickening (Volchkov *et al.* 1973), the correlation remained reliable across a broad range of conditions. In contrast, Phalnikar's widely used relation (Phalnikar, Kumar & Alvi 2008), which estimates the supersonic core length as $SCL^* = 1.8\eta_0 + 2.9$, showed significant errors in predicting the normalised potential core length, as shown in table 6. Although the supersonic core extends slightly beyond the potential core, their difference is minor, making it a reasonable comparison metric. However, Phalnikar's relation, derived from empirical data with NPR less than 8, fails at higher NPR values due to unaccounted changes in shockwave structures and flow regimes. By capturing these effects, the present correlation provides a more accurate representation across a wider range of supersonic free jets, including extremely under-expanded free jets with high pressure ratios and one-barrel shockwaves (Fond *et al.* 2018; Bykov *et al.* 2023).

Author (measurement technique)	Fond <i>et al.</i> (PIV)	Present (MTV)	Bykov <i>et al.</i> (DSMC)
Flow regime	Turbulent	Laminar	Transition (laminar to scattering)
Total pressure (P_0)	120 bar	128 torr	150 torr
Total temperature (T_0)	273 K	300 K	309.5 K
Nozzle pressure ratio (η_0)	120	128	6979
Critical (outlet) Reynolds number (Re_*)	$> 4.0 \times 10^5$	4.53×10^3	2.5×10^3
Complex Reynolds number (Re_L)	$> 3.6 \times 10^4$	4.00×10^2	3.0×10^1
PCL^* (experiment or simulation data)	~ 35	~ 120	~ 120
PCL^* (present correlation)	35.6	107	109
SCL^* (Phalnikar <i>et al.</i> relation)	219	233	12 565

Table 6. Comparison of potential core length.

5. Conclusion

Previous research into supersonic jet flows occurring in rarefied gas conditions has focused predominantly on the near-field zone, with limited emphasis on quantitative flow velocity measurement or analysis in the far-field zone. However, flow characteristics in the far-field zone undergo substantial changes, necessitating a thorough understanding of their behaviour.

In this study, we established a robust experimental foundation for understanding the flow field of a rarefied supersonic free jet within the laminar and turbulent flow regimes, encompassing both near-field and far-field zones. Utilising nanometre-sized tracer particles for particle image velocimetry (PIV), and acetone molecules for molecular tagging velocimetry (MTV), distinct flow characteristics were revealed. In the highly under-expanded regime characterised by turbulent flow, the supersonic jet exhibited a cyclical shockwave structure in the near-field zone, followed by a relatively short potential core region. The far-field zone exhibited the spreading rate, decay constant and turbulence statistics of a turbulent jet, and additionally satisfied self-similarity. As the nozzle pressure ratio (NPR) increased, the near-field zone exhibited a single-barrel shockwave structure, while the far-field zone transitioned into a laminar flow regime, consistent with theoretical predictions based on complex Reynolds numbers. The velocity near the Mach disk significantly decreased, and the shear layer developed slowly in the laminar flow regime, resulting in an extended potential core region. Beyond the potential core, a fully-developed region was reached, satisfying self-similarity in accordance with laminar jet theory. Additionally, we modelled the velocity profile after the Mach disk with a one-barrel shockwave structure in the laminar flow regime using a bi-modal distribution. This was found to accurately replicate the inner and outer shear layers, and merges into a normal distribution after the shear layers converge. Through this analysis, we developed a new correlation to estimate the potential core length based on NPR and complex Reynolds number.

The significance of this work is fourfold. First, the experiments represent the first quantitative measurement of the velocity profile in the far-field zone of a supersonic free jet in rarefied conditions utilising MTV. Second, this study provides experimental evidence of the inability of particles to accurately follow supersonic flow in rarefied environments by quantitatively comparing PIV and MTV results. This demonstrates that relying solely on the Stokes number at the nozzle outlet is insufficient for determining the applicability of PIV in such conditions. Third, the theoretical significance is highlighted by the observation and modelling of a long annular shear layer developing in the laminar flow

regime following the Mach disk. This deviation from typical turbulent jet characteristics underscores the necessity for a more thorough understanding of flow dynamics in extreme environments. Fourth, from an application perspective, these findings provide insights for designing key devices in semiconductor and aerospace industries, such as showerheads, micro-throttles or lunar landing systems.

Looking ahead, future work will focus on expanding the scope of this research to encompass multi-hole jet configurations. Considering that many applications have multiple jets originating from several outlets, understanding jet-to-jet interaction is crucial for capturing the complexities of supersonic free jets. As shockwave structures become more intricate, the influence of multi-hole configurations on the far-field flow dynamics must also be thoroughly investigated.

Funding. This work was supported by the National Research Foundation of Korea (NRF) grant funded by the Korea government (MSIT) (No. RS-2024-00346766 and RS-2024-00406514) and Samsung Electronics (RRH0120ZZ-04RF). Additionally, this work was supported by the Institute of Advanced Machines and Design, and the Institute of Engineering Research at Seoul National University.

Declaration of interests. The authors report no conflict of interest.

Author contributions. H.P.: conceptualisation, data curation, formal analysis, investigation, methodology, software, validation, visualisation, writing – original draft. S.L.: data curation, formal analysis, methodology, software. W.H.: project administration, funding acquisition, resources, supervision, writing – review and editing.

Data availability statement. All relevant data are within the paper.

Appendix A. Derivation of complex Reynolds number in major regions of the jet

Based on the research of Volchkov *et al.* (1973), we can define a Reynolds number at each major area in the extremely under-expanded supersonic free jet depicted in figure 1(b). The flow field is delineated into three main areas: the zone of silence before the Mach disk (region 1), the area following the Mach disk (region 2), and the annular shear layer unaffected by the Mach disk (region 3).

In region 1, the jet core region, bounded by the barrel shock and the Mach disk, the variation of the viscosity coefficient with temperature follows $\mu \sim T^w$, where μ represents the dynamic viscosity, T is the static temperature, and w is an exponent defining the temperature dependence. In this zone, the density ρ_1 near the jet axis and far from the nozzle where the velocity u_1 approaches its maximum is given by $\rho_1/\rho_0 = BD_e^2/x^2$, where ρ_0 is the density in the nozzle's forechamber, x is the distance from the nozzle outlet, and $B = B(\gamma, M)$ is a coefficient dependent on the specific heat ratio γ and Mach number M . The characteristic length scale in this region, represented by the distance to the Mach disk L_M , is expressed as $L_M = 0.67D_e\sqrt{\eta_0}$, where D_e is the nozzle diameter, and η_0 is the pressure ratio between the total pressure P_0 and the ambient pressure P_∞ (Sherman 1966). The Reynolds number in region 1, denoted as Re_1 , is calculated using $Re_1 \sim M^{2w} Re_*/\sqrt{\eta_0}$, where Re_* is the Reynolds number based on the nozzle throat diameter. Dissipative effects are characterised by the local Knudsen number, defined as $Kn_1 \sim \sqrt{\eta_0}/Re_*$. The dimensionless parameter $Re_*/\sqrt{\eta_0}$ is useful for analysing the effects of viscosity, thermal conduction and molecular energy relaxation processes in the jet core.

In region 2 after the Mach disk, the characteristic dimension is the Mach disk diameter D_M , and the Reynolds number in this region is calculated as $Re_2 \sim \rho_2 u_2 D_M/\mu_2$, where ρ_2 represents the average density, u_2 is the average velocity, and μ_2 is the average dynamic viscosity in region 2. For large pressure ratios ($\eta_0 \gg 1$), the approximations $\mu_2 \sim \mu_e$, $u_2 \sim$

u_e/U_{max} and $\rho_2 \sim (\gamma + 1)B\rho_0 D_e^2/(\gamma - 1)L_M^2$ hold true. Given that $D_M \sim D_e\sqrt{\eta_0}$ and $L_M \sim D_e\sqrt{\eta_0}$, the Reynolds number simplifies to $Re_2 \sim Re_*/\sqrt{\eta_0}$.

Finally, in region 3, which refers to the mixing layer after the barrel shock, the Reynolds number is defined as $Re_3 \sim \rho_3 u_3 \Delta/\mu_3$, where ρ_3 is the average density, u_3 is the average velocity, Δ is the thickness, and μ_3 is the average dynamic viscosity of the mixing layer. At large distances from the nozzle, where the annular layer dominates the flow rate, the continuity equation helps to approximate $\rho_3 u_3 \sim \rho_e u_e D_e^2/D_M \Delta$. Given that $D_M \sim D_e\sqrt{\eta_0}$ and $\Delta \sim D_e\sqrt{\eta_0}$, we obtain $Re_3 \sim \mu_0 Re_*/\mu_3\sqrt{\eta_0}$. This leads to $Re_3 \sim (T_0/T_3)^w Re_*/\sqrt{\eta_0}$, where T_0 is the stagnation temperature, and T_3 is the static temperature in the mixing layer. For congruent cross-sections where $T_0 \approx T_3$, the Reynolds number simplifies to $Re_3 \sim Re_*/\sqrt{\eta_0}$.

In conclusion, for all three zones, the local Reynolds numbers consistently scale with $Re_*/\sqrt{\eta_0}$, making this ratio the fundamental criterion for describing viscosity, thermal conduction and relaxation effects.

Appendix B. Thermophysical property variation

In this appendix, the influence of the variation in thermophysical properties resulting from seeding acetone as a tracer molecule for the MTV experiments in quasi-vacuum conditions is examined. The MTV technique is widely employed in fluid mechanics research, which provides valuable insights into velocity profiles and flow characteristics. However, the addition of acetone as seed introduces complexities due to the distinct thermophysical properties compared to the base gas of nitrogen used in the experiments. To accurately interpret the MTV data and account for the effects of acetone seeding, a comprehensive understanding of the variation in thermophysical properties is essential.

Some studies (Handa *et al.* 2011; Sakurai *et al.* 2015) have controlled the acetone concentration to below 1 % and assumed minimal impact from seeding. However, typically when seeding acetone using a bubbler or aerosol generator, it is challenging to precisely determine the concentration. Thus prior studies (Huffman & Elliott 2009; Gragston & Smith 2022; Andrade *et al.* 2022) utilising acetone have assumed full saturation at the given total temperature and pressure, and analysed the effect of maximum acetone seeding. In our study, we also assumed full saturation and analysed its effects.

First, the saturated pressure at 300 K was calculated using the Antoine equation below and is shown in figure 32, with seeding performed at 300 K and 760 torr in an N₂ positive chamber:

$$P_{sat} = 10^{7.13-1220(T-43)}, \tag{B1}$$

where P_{sat} is acetone saturated vapour pressure (torr), and T is temperature (K). Based on this equation, the N₂ to acetone gas ratio was found to be 67 : 33, allowing calculation of the mixture's specific heat using Dalton's law:

$$C_{p,mix} = m_{C_3H_6O} C_{p,C_3H_6O} + (1 - m_{C_3H_6O}) C_{p,N_2}, \tag{B2}$$

$$C_{v,mix} = m_{C_3H_6O} C_{v,C_3H_6O} + (1 - m_{C_3H_6O}) C_{v,N_2}, \tag{B3}$$

where C_p and C_v are constant pressure and volume specific heats, respectively, and m is mole fraction of the species. Additionally, density and dynamic viscosity were calculated to obtain the mixture density and dynamic viscosity (Faghri & Zhang 2006), crucial for understanding the influence of acetone on the complex Reynolds number. Following acetone seeding, as seen in table 7, the specific heat ratio slightly decreased to 1.3, remaining constant at both 10 and 1 torr. The complex Reynolds number, as shown in table 8, slightly increased from 1300 to 1400 at 10 torr, and from 400 to 430 at 1 torr.

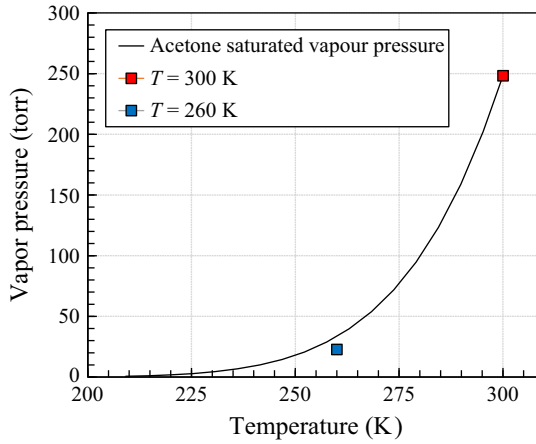


Figure 32. Acetone saturated vapour pressure calculated from the Antoine equation.

Parameters	Nitrogen	Acetone (gas)	Mixture (67 % N ₂ : 33 % acetone)
Gas constant R (J K ⁻¹ Kg ⁻¹)	287	143	251
Specific heat C _p (J K ⁻¹ Kg ⁻¹)	1005	1290	1076
Specific heat C _v (J K ⁻¹ Kg ⁻¹)	718	1147	825
Specific heat ratio	1.4	1.13	1.3
Density (kg m ⁻³)	0.115	0.1	0.11
Dynamic viscosity (Pa s)	1.548 × 10 ⁻⁵	7.300 × 10 ⁻⁶	1.278 × 10 ⁻⁵
Kinematic viscosity (m ² s ⁻¹)	1.346 × 10 ⁻⁴	7.300 × 10 ⁻⁵	1.162 × 10 ⁻⁴

Table 7. Thermophysical property variation with acetone seeding.

Chamber pressure, P _∞ (Reservoir pressure, P ₀)	10 torr (121 torr)	1 torr (128 torr)
Flow regime	Turbulent (continuum)	Laminar (continuum)
Critical Reynolds number (without acetone seeding)	4.53 × 10 ³	4.53 × 10 ³
Complex Reynolds number (without acetone seeding)	1.30 × 10 ³	4.00 × 10 ²
Critical Reynolds number (with acetone seeding)	4.72 × 10 ³	4.72 × 10 ³
Complex Reynolds number (with acetone seeding)	1.40 × 10 ³	4.30 × 10 ²

Table 8. Reynolds number variation with acetone seeding.

However, these variations had minimal impact on the jet flow regime, with little change observed in spreading rates, particularly in the laminar flow regime.

Appendix C. Evolution of the Stokes number in the zone of silence

The Stokes number is defined as τ_p/τ_f , where τ_p is the particle relaxation time scale, and τ_f is a fluid time scale. The particle relaxation time scale is defined as

$$\tau_p = \frac{\rho_p d_p^2}{18\mu_f}, \quad (C1)$$

where ρ_p , d_p and μ_f are the particle density, diameter and fluid dynamic viscosity, respectively. In the case of the fluid time scale, it can be obtained using the mean velocity magnitude at the nozzle outlet and nozzle diameter.

To account for the rarefied gas conditions in the downstream region, the Cunningham correction factor (Cunningham 1910; Davies 1945) C_c is used to correct the Stokes number, taking into account the molecular mean free path as a constant multiplier that is defined as

$$C_c = 1 + \frac{2\lambda_\infty}{d_p} \left[1.257 + 0.4 \exp\left(\frac{-1.1d_p}{2\lambda_\infty}\right) \right]. \quad (C2)$$

The molecular mean free path (λ_∞) is given by

$$\lambda_\infty = \frac{\mu_f}{P} \sqrt{\frac{\pi k_B T}{2m}}, \quad (C3)$$

where P , k_B , T and m are static pressure, Boltzmann constant, static temperature and molecular mass, respectively. In the zone of silence up to the Mach disk, the normalised static temperature and pressure can be computed using equations provided by Morse (1996). Additionally, fluid dynamic viscosity was determined using the NIST Standard Reference Database (Linstrom *et al.* 2005). These values allowed for the calculation of the mean free path as a function of normalised streamwise distance, which was then used to compute the Cunningham correction factor. The local Stokes number, incorporating the Cunningham correction factor, is expressed as

$$Stk_c = Stk \times C_c = \frac{\tau_p}{\tau_f} \times C_c = \frac{\rho_p d_p^2 / 18\mu_f}{D_{x^*} / V_{x^*}} \times C_c, \quad (C4)$$

where D_{x^*} is the characteristic length at x^* , and V_{x^*} is the characteristic velocity at x^* . To determine the fluid time scale, the characteristic length and velocity were derived based on mass conservation, as there is no entrainment flow in the zone of silence:

$$\rho_e D_e V_e \sim \rho_{x^*} D_{x^*} V_{x^*}. \quad (C5)$$

Here, ρ_e , D_e , V_e and ρ_{x^*} denote exit density, nozzle diameter, exit velocity and density at x^* , respectively. The density at x^* was calculated using relations from Morse (1996), while V_{x^*} was defined as the centreline velocity, which increases spherically with distance from the nozzle outlet. The final expression for the Stokes number, incorporating the Cunningham correction factor, is given by

$$Stk_c = \frac{\rho_p d_p^2 / 18\mu_f}{\rho_e D_e V_e / (\rho_{x^*} V_{x^*}^2)} \times C_c. \quad (C6)$$

Using this equation, the variation of the local Stokes number with normalised streamwise distance is shown in figure 33. A rapid increase in the local Stokes number is observed shortly after the jet discharge. Exceeding unity at $x^* \sim 2$, this indicates that PIV tracers fail to accurately follow the flow beyond this point.

Most prior studies (Schrijer, Scarano & Van Oudheusden 2006; Mitchell, Honnery & Soria 2013; De Gregorio 2014; André *et al.* 2014; Edgington-Mitchell *et al.* 2014a) on supersonic free jets have involved NPR below 10, where x^* typically remains below 2, allowing successful PIV measurements. Even in cases with NPR exceeding 100, such

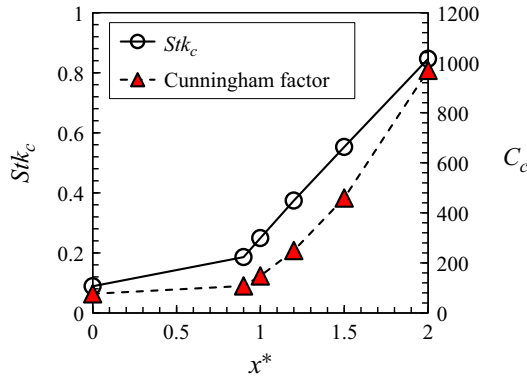


Figure 33. Evolution of local Stokes number and Cunningham factor in the zone of silence.

as the jet operating at total pressure 120 bar studied by Fond *et al.* (2018), the mean free path was small enough for PIV to succeed. However, in the current study, with NPR exceeding 100 and operating in a rarefied environment, the local Stokes number increases exponentially, which makes it very difficult for PIV tracers to follow the flow accurately. This observation aligns with findings from prior research (Huffman & Elliott 2009; Glazyrin, Mursenkova & Znamenskaya 2015; Sakurai *et al.* 2015; Williams *et al.* 2015).

Appendix D. Proper orthogonal decomposition analysis

In this appendix, proper orthogonal decomposition (POD) analysis is conducted to understand the primary dominant flow structure in the free jet. The analysis is based on the instantaneous velocity field utilising PIV experimental data obtained from turbulent flow regimes of free jets at 10 torr.

D.1. Methodology

POD analysis is a powerful technique for reducing spatially complicated flow fields to a manageable amount of spatial modes and their temporal coefficients (Taira *et al.* 2017, 2020). The POD calculates a minimal set of orthogonal basis functions that contain enough information to describe the original system dynamics. In other words, by linear summation of basis modes, the ensemble can be reconstructed approximately.

In order to apply POD analysis in this study, we defined the function $\tilde{\mathbf{x}}(\boldsymbol{\xi}, t)$ as the instantaneous velocity field of PIV data, where $\boldsymbol{\xi}$ denotes the Cartesian spatial coordinates (e.g. (x, y) in a planar field), and t represents time. We first separate the data into average and fluctuating components:

$$\tilde{\mathbf{x}}(\boldsymbol{\xi}, t) = \bar{\mathbf{x}}(\boldsymbol{\xi}) + \mathbf{x}(\boldsymbol{\xi}, t), \tag{D1}$$

where $\bar{\mathbf{x}}$ is the ensemble average, and \mathbf{x} is the fluctuation component. The fluctuation component \mathbf{x} can be decomposed mathematically into spatial and temporal functions as

$$\mathbf{x}(\boldsymbol{\xi}, t) \approx \sum_{j=1}^N c_j(t) \boldsymbol{\phi}_j(\boldsymbol{\xi}), \tag{D2}$$

where $\phi_j(\xi)$ is the POD spatial mode, $c_j(t)$ is the corresponding temporal coefficient for mode j , and N is the number of modes. Here, N theoretically approaches infinity, but in practice it is taken as the number of snapshots or modes used for reconstruction. In addition, spatial modes are a set of orthogonal modes defined as

$$\int_V \phi_i(\xi) \cdot \phi_j(\xi) dV = \delta_{ij}, \quad i, j = 1, 2, \dots, N, \quad (D3)$$

where V is the spatial domain. To compute the POD modes, a set of m snapshots $\mathbf{x}(t_i) = \tilde{\mathbf{x}}(\xi, t) - \bar{\mathbf{x}}(\xi) \in \mathbb{R}^n$ is assembled into a snapshot matrix $\mathbf{X} = [\mathbf{x}(t_1), \mathbf{x}(t_2), \dots, \mathbf{x}(t_m)] \in \mathbb{R}^{n \times m}$. The covariance matrix is defined as

$$\mathbf{R} = \mathbf{X}\mathbf{X}^T \in \mathbb{R}^{n \times n}. \quad (D4)$$

Due to the high dimensionality of \mathbf{R} , the method of snapshots (Sirovich 1987) is employed by solving the reduced eigenvalue problem. This approach recognises that the non-zero eigenvalues of $\mathbf{R} = \mathbf{X}\mathbf{X}^T$ are the same as those of the smaller $\mathbf{X}^T\mathbf{X} \in \mathbb{R}^{m \times m}$. We therefore solve the eigenvalue problem of size m :

$$\mathbf{X}^T\mathbf{X}\boldsymbol{\psi}_j = \lambda_j\boldsymbol{\psi}_j, \quad (D5)$$

where $\boldsymbol{\psi} \in \mathbb{R}^m$ represents the eigenvector associated with the eigenvalue λ_j in the reduced space. Once this smaller problem is solved, the spatial POD mode is recovered by combining the snapshots using $\boldsymbol{\psi}_j$ as weights:

$$\phi_j = \frac{1}{\sqrt{\lambda_j}}\mathbf{X}\boldsymbol{\psi}_j. \quad (D6)$$

This approach is mathematically equivalent to performing a singular value decomposition of \mathbf{X} , where singular values σ_j relate to POD energy $\lambda_j = \sigma_j^2$.

D.2. Cumulative total energy and spatial feature with POD mode

The magnitude of the eigenvalue represents the energy of the POD mode. Thus we can quantify the fraction of energy in the dataset of the n th POD mode as

$$\text{kinetic energy fraction} = \lambda_n / \sum_{i=1}^N \lambda_i. \quad (D7)$$

The kinetic energy fraction and normalised cumulative energy results for a supersonic free jet at 10 torr are presented in figure 34. The near-field zone of the 10 torr free jet features shockwaves, making PIV experimental data unavailable. However, from $x/D_e = 30$ onwards, where shockwaves are absent and self-similarity is satisfied, PIV experimental data align with the MTV data, prompting POD analysis. This analysis aims to unveil turbulent flow structures in the 10 torr free jet. Dominant modes 1–10 encapsulate approximately 20 % of the energy, with mode 1 holding 12 % of the energy, and the turbulent effects are distributed in the subsequent modes.

We examined the eigenfunctions of the dominant modes to understand specific spatial features. Figure 35 depicts the eigenfunctions of the primary modes in the streamwise and spanwise directions, respectively. In modes 1 and 2, the flow exhibits the development of a prominent shear layer, wherein opposing velocity streams converge, leading to the formation of large-scale coherent vortex structures. Conversely, mode 3 is characterised by the shedding of small-scale eddies, which influence flow stability.

The POD analysis of the far-field zone for the 10 torr free jet exhibits turbulent flow structures, providing direct evidence that the flow did not transition back to a stable laminar flow regime.

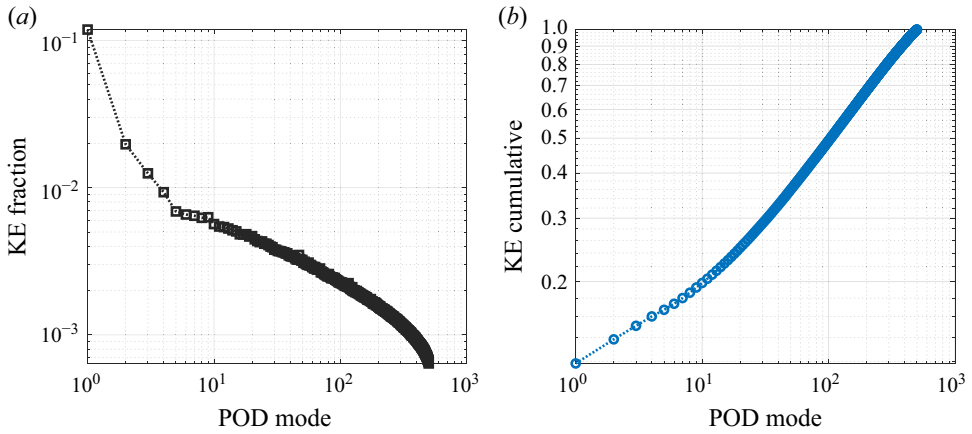


Figure 34. (a) Kinetic energy (KE) fraction and (b) cumulative total energy plot with POD mode at 10 torr (PIV).

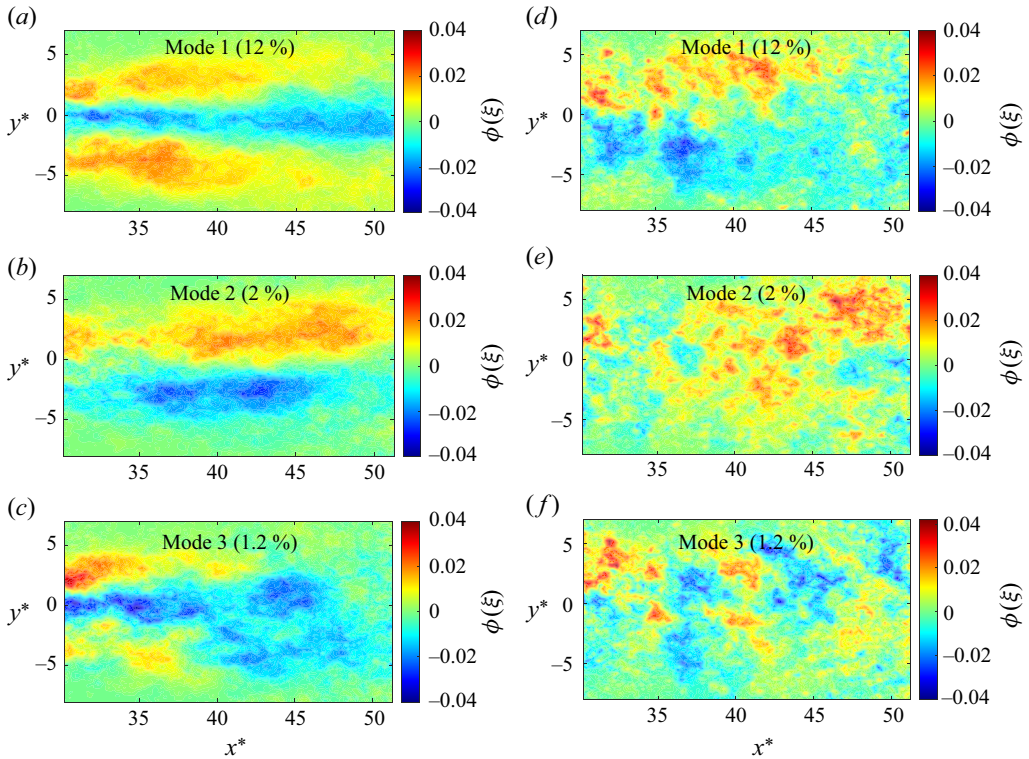


Figure 35. Streamwise eigenfunction contours for (a) mode 1, (b) mode 2, and (c) mode 3. Spanwise eigenfunction contour for (d) mode 1, (e) mode 2, and (f) mode 3.

Appendix E. Comparison between PIV and MTV in an extremely under-expanded supersonic free jet

The findings confirm that MTV adequately measures flow velocities, at least within the near-field zone. To further investigate the difference between MTV and PIV results, the

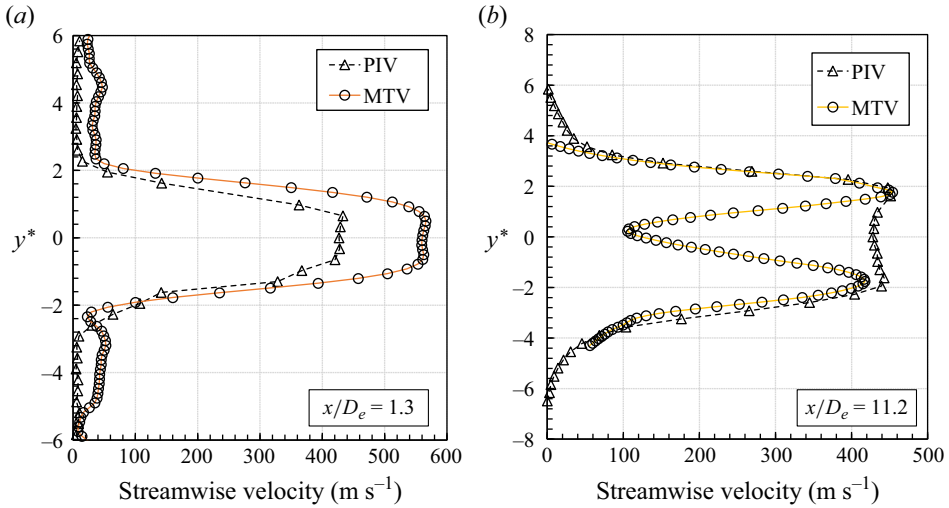


Figure 36. Comparison of streamwise mean velocity profiles in the near-field zone between MTV and PIV at (a) $x/D_e = 1.3$ and (b) $x/D_e = 11.2$.

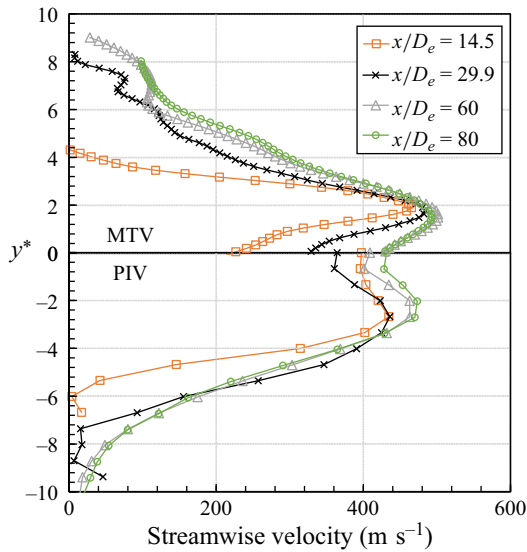


Figure 37. Streamwise mean velocity profile comparison between MTV and PIV in potential core region and far-field zone.

streamwise mean velocity profile is depicted in [figure 36](#). As is evident from [figure 36\(a\)](#), PIV fails to measure the velocity profile at the nozzle exit, due to abrupt density changes. However, the overall shape of the flow profile remains similar. Examining the flow beyond the Mach disk in [figure 36\(b\)](#), MTV results show a sharp velocity decrease in the central region, contrary to the PIV results. As explained for the 10 torr case, the curvature of the Mach disk causes only the central part to act as a normal shockwave, with weaker shocks in surrounding areas. This leads to significant velocity reduction at the centre. Interestingly, while PIV does not capture the velocity decrease induced by the Mach disk, it closely aligns with MTV at the shear layer region surrounding the Mach disk. This implies that

the diameter of the Mach disk can be inferred from the distance between the two peaks, which indeed matches closely with theoretical value $D_{Mach}/D_e = 3.2$.

To investigate the development of the mixing layer, we compared MTV and PIV results, which are displayed in figure 37. Both plots show the development of the inner and outer shear layers as they move downstream. However, PIV results do not fully capture the effects induced by the Mach disk, resulting in a slight decrease followed by an increase in the centreline streamwise mean velocity. Additionally, the rate of increase in velocity near the centreline is initially faster in the MTV results, gradually decreasing over distance. This indicates that after the Mach disk, strong shear induced by the velocity gradient leads to a rapid increase in velocity, which then diminishes downstream as the velocity gradient decreases due to the weakening of the shear layer.

REFERENCES

- ANDRADE, A., HOFFMAN, E.N.A., LALONDE, E.J. & COMBS, C.S. 2022 Velocity measurements in a hypersonic flow using acetone molecular tagging velocimetry. *Opt. Express* **30** (23), 42199–42213.
- ANDRÉ, B., CASTELAIN, T. & BAILLY, C. 2014 Investigation of the mixing layer of underexpanded supersonic jets by particle image velocimetry. *Intl J. Heat Fluid Flow* **50**, 188–200.
- BAJPAI, A., BHATEJA, A. & KUMAR, R. 2024 Plume–surface interaction during lunar landing using a two-way coupled DSMC–DEM approach. *Phys. Rev. Fluids* **9** (2), 024306.
- BALL, C.G., FELLOUAH, H. & POLLARD, A. 2012 The flow field in turbulent round free jets. *Prog. Aerosp. Sci.* **50**, 1–26.
- BELAN, M., DE PONTE, S. & TORDELLA, D. 2008 Determination of density and concentration from fluorescent images of a gas flow. *Exp. Fluids* **45** (3), 501–511.
- BELAN, M., DE PONTE, S., TORDELLA, D., MASSAGLIA, S., MIGNONE, A., BODENSCHATZ, E. & FERRARI, A. 2011 Hydrodynamics of hypersonic jets: experiments and numerical simulations. *Astrophys. Space Sci.* **336** (1), 9–14.
- BIRCH, A.D., HUGHES, D.J. & SWAFFIELD, F. 1987 Velocity decay of high pressure jets. *Combust. Sci. Technol.* **52** (1–3), 161–171.
- BURATTINI, P., ANTONIA, R.A. & DANAILA, L. 2005 Similarity in the far field of a turbulent round jet. *Phys. Fluids* **17** (2), 025101.
- BYKOV, N.Y., GORBACHEV, Y.E. & FYODOROV, S.A. 2023 Highly underexpanded rarefied jet flows. *Front. Mech. Engng* **9**, 1216927.
- CAPECELATRO, J. & WAGNER, J.L. 2024 Gas–particle dynamics in high-speed flows. *Annu. Rev. Fluid Mech.* **56** (1), 379–403.
- CRIST, S., GLASS, D.R. & SHERMAN, P.M. 1966 Study of the highly underexpanded sonic jet. *AIAA J.* **4** (1), 68–71.
- CUESTA, C.J., DAVIES, J., WORRALL, K., CAMMARANO, A. & ZARE-BEHTASH, H. 2025 Plume–surface interactions: a review of experimental work. *Acta Astronaut.* **226**, 892–912.
- CUNNINGHAM, E. 1910 On the velocity of steady fall of spherical particles through fluid medium. *Proc. R. Soc. Lond. A* **83** (563), 357–365.
- DAVIES, C.N. 1945 Definitive equations for the fluid resistance of spheres. *Proc. Phys. Soc.* **57** (4), 259–270.
- DE GREGORIO, F. 2014 Free compressible jet investigation. *Exp. Fluids* **55**, 1–21.
- DETTLEFF, G. 1991 Plume flow and plume impingement in space technology. *Prog. Aerosp. Sci.* **28** (1), 1–71.
- DETTLEFF, G. & GRABE, G. 2011 Basics of plume impingement analysis for small chemical and cold gas thrusters. In *Proceedings of the Models and Computational Methods for Rarefied Flows*, RTO/NATO, 1–40.
- DUBROVIN, K.A., ZARVIN, A.E., KALYADA, V.V. & YASKIN, A.S. 2023 Influence of the outflow initial parameters on the transverse dimensions of underexpanded argon jets in presence of condensation. *Vacuum* **207**, 111651.
- DULOV, V.G. & LUK'YANOV, G.A. 1984 Gas Dynamics of Outflow Processes [in Russian], Nauka, Novosibirsk, 235.
- EDGINGTON-MITCHELL, D., HONNERY, D.R. & SORIA, J. 2014a The underexpanded jet Mach disk and its associated shear layer. *Phys. Fluids* **26** (9), 096101.
- EDGINGTON-MITCHELL, D., OBERLEITHNER, K., HONNERY, D.R. & SORIA, J. 2014b Coherent structure and sound production in the helical mode of a screeching axisymmetric jet. *J. Fluid Mech.* **748**, 822–847.
- FAGHRI, A. & ZHANG, Y. 2006 *Transport Phenomena in Multiphase Systems*. Elsevier.

- FOND, B., XIAO, C.-N., T'JOEN, C., HENKES, R., VEENSTRA, P., VAN WACHEM, B.G.M. & BEYRAU, F. 2018 Investigation of a highly underexpanded jet with real gas effects confined in a channel: flow field measurements. *Exp. Fluids* **59** (10), 1–21.
- FRANQUET, E., PERRIER, V., GIBOUT, S. & BRUEL, P. 2015 Free underexpanded jets in a quiescent medium: a review. *Prog. Aerosp. Sci.* **77**, 25–53.
- FRATANTONIO, D., ROJAS-CÁRDENAS, M., BARROT, C., BALDAS, L. & COLIN, S. 2020 Velocity measurements in channel gas flows in the slip regime by means of molecular tagging velocimetry. *Micromachines-BASEL* **11** (4), 374.
- FRATANTONIO, D., ROJAS-CÁRDENAS, M., MOHAND, H.S.H., BARROT, C., BALDAS, L. & COLIN, S. 2018 Molecular tagging velocimetry for confined rarefied gas flows: phosphorescence emission measurements at low pressure. *Exp. Therm. Fluid Sci.* **99**, 510–524.
- GARCIA, A.L., MANSOUR, M.M., LIE, G.C., MARESCHAL, M. & CLEMENTI, E. 1987 Hydrodynamic fluctuations in a dilute gas under shear. *Phys. Rev. A* **36** (9), 4348–4355.
- GENDRICH, C.P. & KOCHESFAHANI, M.M. 1996 A spatial correlation technique for estimating velocity fields using molecular tagging velocimetry (MTV). *Exp. Fluids* **22** (1), 67–77.
- GLAZYRIN, F.N., MURSENKOVA, I.V. & ZNAMENSKAYA, I.A. 2015 PIV tracer behavior on propagating shock fronts. *Meas. Sci. Technol.* **27** (1), 015302.
- GORMAN, M.T., RUBIO, J.S., DIAZ-LOPEZ, M.X., CHAMBERS, W.A., KORZUN, A.M., RABINOVITCH, J. & NI, R. 2023 Scaling laws of plume-induced granular cratering. *PNAS Nexus* **2** (9), pgad300.
- GRAGSTON, M. & SMITH, C.D. 2022 10 kHz molecular tagging velocimetry in a Mach 4 air flow with acetone vapor seeding. *Exp. Fluids* **63** (5), 85.
- GRAUR, I.A., ELIZAROVA, T.G., RAMOS, A., TEJEDA, G., FERNÁNDEZ, J.M. & MONTERO, S. 2004 A study of shock waves in expanding flows on the basis of spectroscopic experiments and quasi-gasdynamic equations. *J. Fluid Mech.* **504**, 239–270.
- HANDA, T., MASUDA, M., KASHITANI, M. & YAMAGUCHI, Y. 2011 Measurement of number densities in supersonic flows using a method based on laser-induced acetone fluorescence. *Exp. Fluids* **50** (6), 1685–1694.
- HANDA, T., MII, K., SAKURAI, T., IMAMURA, K., MIZUTA, S. & ANDO, Y. 2014 Study on supersonic rectangular microjets using molecular tagging velocimetry. *Exp. Fluids* **55** (5), 1–9.
- HASH, D.B., MIHOPOULOS, T., GOVINDAN, T.R. & MEYAPPAN, M. 2000 Characterization of showerhead performance at low pressure. *J. Vac. Sci. Technol. B*, **18** (6), 2808–2813.
- HUFFMAN, R. & ELLIOTT, G. 2009 An experimental investigation of accurate particle tracking in supersonic, rarefied, axisymmetric jets. In *47th AIAA Aerospace Sciences Meeting Including The New Horizons Forum and Aerospace Exposition*, p. 1265. AIAA.
- HUSSEIN, H.J., CAPP, S.P. & GEORGE, W.K. 1994 Velocity measurements in a high-Reynolds-number, momentum-conserving, axisymmetric, turbulent jet. *J. Fluid Mech.* **258**, 31–75.
- INMAN, J., DANEHY, P., NOWAK, R. & ALDERFER, D. 2008 Identification of instability modes of transition in underexpanded jets. In *38th Fluid Dynamics Conference and Exhibit*, p. 4389. AIAA.
- International Organization for Standardization (ISO), International Organization of Legal Metrology (OIML) & Bureau International des Poids et Mesures (BIPM) 2009 Guide to the expression of uncertainty in measurement. Madrid: AENOR; Geneva: ISO.
- JERÓNIMO, A., RIETHMULLER, M.L. & CHAZOT, O. 2002 PIV application to Mach 3.75 overexpanded jet. In *Proceedings 11th International Symposium on Application of Laser Techniques to Fluid Mechanics*.
- JIANG, C., HAN, T., HU, S., GAO, Z. & LEE, C.-H. 2022 Theoretical prediction for the Mach-disk height in two-dimensional supersonic underexpanded jets. *AIAA J.* **60** (4), 2115–2129.
- KASHI, B., WEINBERG, E. & HAUSTEIN, H.D. 2018 Analytical re-examination of the submerged laminar jet's velocity evolution. *Phys. Fluids* **30** (6), 063604.
- KISLYAKOV, N.I., REBROV, A.K. & SHARAFUTDINOV, R.G. 1975 Structure of high-pressure low-density jets beyond a supersonic nozzle. *J. Appl. Mech. Tech. Phys.* **16** (2), 187–195.
- KOSOV, A.V., REBROV, A.K. & SHARAFUTDINOV, R.G. 1980 Ejecting action of a high-pressure low-density free jet. *Vacuum* **30** (8–9), 301–305.
- LEMPERT, W.R., BOEHM, M., JIANG, N., GIMELSHEIN, S. & LEVIN, D. 2003 Comparison of molecular tagging velocimetry data and direct simulation Monte Carlo simulations in supersonic micro jet flows. *Exp. Fluids* **34** (3), 403–411.
- LEMPERT, W.R., JIANG, N., SETHURAM, S. & SAMIMY, M. 2002 Molecular tagging velocimetry measurements in supersonic microjets. *AIAA J.* **40** (6), 1065–1070.
- LEWIS, J.R., CLARKE, H. & CARLSON, D.J. 1964 Normal shock location in underexpanded gas and gas-particle jets. *AIAA J.* **2** (4), 776–777.

- LI, J., CAI, J., WU, Z., WANG, J., PEI, Y. & WANG, G. 2019 Numerical simulation and study of the metal-organic chemical vapor deposition growth of ZnO film. *Phys. Fluids* **31** (2), 027104.
- LINSTROM, P.J. & MALLARD, W.G. (Eds) NIST Chemistry WebBook, NIST Standard Reference Database Number 69, National Institute of Standards and Technology, Gaithersburg MD, 20899.
- LOTH, E., TYLER DASPIT, J., JEONG, M., NAGATA, T. & NONOMURA, T. 2021 Supersonic and hypersonic drag coefficients for a sphere. *AIAA J.* **59** (8), 3261–3274.
- MANSOUR, M.M., GARCIA, A.L., LIE, G.C. & CLEMENTI, E. 1987 Fluctuating hydrodynamics in a dilute gas. *Phys. Rev. Lett.* **58** (9), 874–877.
- MATE, B., GRAUR, I.A., ELIZAROVA, T., CHIROKOV, I., TEJEDA, G., FERNÁNDEZ, J.M. & MONTERO, S. 2001 Experimental and numerical investigation of an axisymmetric supersonic jet. *J. Fluid Mech.* **426**, 177–197.
- MEHTA, M., SENGUPTA, A., RENNO, N.O., NORMAN, J.W.V., HUSEMAN, P.G., GULICK, D.S. & POKORA, M. 2013 Thruster plume surface interactions: applications for spacecraft landings on planetary bodies. *AIAA J.* **51** (12), 2800–2818.
- MITCHELL, D.M., HONNERY, D.R. & SORIA, J. 2013 Near-field structure of underexpanded elliptic jets. *Exp. Fluids* **54** (7), 1–13.
- MORSE, M.D. 1996 Supersonic beam sources. *Exp. Meth. Phys. Sci.* **29**, 21–47.
- MORTON, B.R. 1967 Entrainment models for laminar jets, plumes, and wakes. *Phys. Fluids* **10** (10), 2120–2127.
- MURPHY, H.R. & MILLER, D.R. 1984 Effects of nozzle geometry on kinetics in free-jet expansions. *J. Phys. Chem.* **88** (20), 4474–4478.
- MUSTAFA, M.A., PARZIALE, N.J., SMITH, M.S. & MARINEAU, E.C. 2017 Nonintrusive freestream velocity measurement in a large-scale hypersonic wind tunnel. *AIAA J.* **55** (10), 3611–3616.
- PANCHAPAKESAN, N.R. & LUMLEY, J.L. 1993 Turbulence measurements in axisymmetric jets of air and helium. Part 1. Air jet. *J. Fluid Mech.* **246**, 197–223.
- PHALNIKAR, K.A., KUMAR, R. & ALVI, F.S. 2008 Experiments on free and impinging supersonic microjets. *Exp. Fluids* **44** (5), 819–830.
- PITZ, R.W. & DANEHY, P.M. 2020 Molecular tagging velocimetry in gases. In *Optical Diagnostics for Reacting and Non-Reacting Flow: Theory and Practice* (ed. A. Steinberg & S. Roy). AIAA.
- PLEMMONS, D.H., MEHTA, M., CLARK, B.C., KOUNAVES, S.P., PEACH, L.L., RENNO, N.O., TAMPPARI, L. & YOUNG, S.M.M. 2008 Effects of the Phoenix Lander descent thruster plume on the Martian surface. *J. Geophys. Res. Planets* **113** (E3), E00A11.
- QUINN, W.R. 2006 Upstream nozzle shaping effects on near field flow in round turbulent free jets. *Eur. J. Mech. B/Fluids* **25** (3), 279–301.
- RAGHEB, A., ELLIOTT, G., CARROLL, D., SOLOMON, W., KING, D. & LAYSTROM-WOODARD, J. 2010 Low pressure schlieren imaging of a multi-stream injection nozzle. In *41st Plasmadynamics and Lasers Conference*, p. 4756. AIAA.
- RAMSEY, M.C. & PITZ, R.W. 2011 Template matching for improved accuracy in molecular tagging velocimetry. *Exp. Fluids* **51** (3), 811–819.
- RANKIN, G.W., SRIDHAR, K., ARULRAJA, M. & KUMAR, K.R. 1983 An experimental investigation of laminar axisymmetric submerged jets. *J. Fluid Mech.* **133**, 217–231.
- REBROV, A.K. 2001 Free jets in vacuum technologies. *J. Vac. Sci. Technol. A*, **19** (4), 1679–1687.
- RODRIGUES, N.S., TYRRELL, O.K. & DANEHY, P.M. 2024 Fluorescence imaging of plume–surface interaction in large-scale reduced pressure environments. *Phys. Fluids* **36** (10), 106146.
- SAKURAI, T., HANDA, T., KOIKE, S., MII, K. & NAKANO, A. 2015 Study on the particle traceability in transonic and supersonic flows using molecular tagging velocimetry. *J. Visual.-Japan* **18** (3), 511–520.
- SCHRIJER, F.F.J., SCARANO, F. & VAN OUDHEUSDEN, B.W. 2006 Application of PIV in a Mach 7 double-ramp flow. *Exp. Fluids* **41** (2), 353–363.
- SCHRÖDER, A., GEISLER, R., OVER, B., GESEMANN, S. & SCHWANE, R. 2011 Measurements of density fields in micro nozzle plumes in vacuum by using an enhanced tomographic background oriented schlieren (BOS) technique. In: *Forum on Developments in Volume Reconstruction Techniques*.
- SCIACCHITANO, A. 2019 Uncertainty quantification in particle image velocimetry. *Meas. Sci. Technol.* **30** (9), 092001.
- SCIACCHITANO, A. & WIENEKE, B. 2016 PIV uncertainty propagation. *Meas. Sci. Technol.* **27** (8), 084006.
- SETYAWAN, H., SHIMADA, M., OHTSUKA, K. & OKUYAMA, K. 2002 Visualization and numerical simulation of fine particle transport in a low-pressure parallel plate chemical vapor deposition reactor. *Chem. Engng Sci.* **57** (3), 497–506.
- SHERMAN, F. 1966 The structure and utilization of supersonic free jets in low density wind tunnels. *Rarefied Gas Dyn.* **2**, 84–105.

- SHURTZ, T.P. & WEST, J. 2022 Simulating underexpanded plumes in Martian and Lunar environments. In *AIAA SCITECH. 2022 Forum*, p. 2318. AIAA.
- SILWAL, L., BHARGAV, V.N., STUBBS, D.C., FULONE, B.K., THUROW, B.S., SCARBOROUGH, D.E. & RAGHAV, V. 2024 Ejecta behavior during plume–surface interactions under rarefied atmospheric conditions. *Acta Astronaut.* **218**, 35–46.
- SIROVICH, L. 1987 Turbulence and the dynamics of coherent structures. I. Coherent structures. *Q. Appl. Maths* **45** (3), 561–590.
- STAMHUIS, E. & THIELICKE, W. 2014 PIVlab – towards user-friendly, affordable and accurate digital particle image velocimetry in Matlab. *J. Open Res. Softw.* **2** (1), 30.
- STEFANOV, S.K., BOYD, I.D. & CAI, C.-P. 2000 Monte Carlo analysis of macroscopic fluctuations in a rarefied hypersonic flow around a cylinder. *Phys. Fluids* **12** (5), 1226–1239.
- SUKESAN, M.K. & SHINE, S.R. 2023 Micronozzle for satellite propulsion and mixture separation: a review. *J. Therm. Anal. Calorim.* **148** (17), 9309–9342.
- TAIRA, K., BRUNTON, S.L., DAWSON, S.T.M., ROWLEY, C.W., COLONIUS, T., MCKEON, B.J., SCHMIDT, O.T., GORDEYEV, S., THEOFILIS, V. & UKEILEY, L.S. 2017 Modal analysis of fluid flows: an overview. *AIAA J.* **55** (12), 4013–4041.
- TAIRA, K., HEMATI, M.S., BRUNTON, S.L., SUN, Y., DURAISAMY, K., BAGHERI, S., DAWSON, S.T.M. & YEH, C.-A. 2020 Modal analysis of fluid flows: applications and outlook. *AIAA J.* **58** (3), 998–1022.
- TEJEDA, G., MATÉ, B., FERNÁNDEZ-SÁNCHEZ, J.M. & MONTERO, S. 1996 Temperature and density mapping of supersonic jet expansions using linear Raman spectroscopy. *Phys. Rev. Lett.* **76** (1), 34–37.
- TROPEA, C., YARIN, A.L. & FOSS, J.F. eds., 2007. *Springer Handbook of Experimental Fluid Mechanics*, vol. 1. Springer.
- VOLCHKOV, V.V., IVANOV, A.V., KISLYAKOV, N.I., REBROV, A.K., SUKHNEV, V.A. & SHARAFUTDINOV, R.G. 1973 Low-density jets beyond a sonic nozzle at large pressure drops. *J. Appl. Mech. Tech. Phys.* **14** (2), 200–207.
- WILLIAMS, O.J.H., NGUYEN, T., SCHREYER, A.-M. & SMITS, A.J. 2015 Particle response analysis for particle image velocimetry in supersonic flows. *Phys. Fluids* **27** (7), 076101.
- WYGNANSKI, I. & FIEDLER, H. 1969 Some measurements in the self-preserving jet. *J. Fluid Mech.* **38** (3), 577–612.
- XIAO, C.-N., FOND, B., BEYRAU, F., T'JOEN, C., HENKES, R., VEENSTRA, P. & VAN WACHEM, B. 2019 Numerical investigation and experimental comparison of the gas dynamics in a highly underexpanded confined real gas jet. *Flow Turbul. Combust.* **103** (1), 141–173.
- XU, G. & ANTONIA, R. 2002 Effect of different initial conditions on a turbulent round free jet. *Exp. Fluids* **33** (5), 677–683.
- YANG, J.Y. & HUANG, J.C. 1995 Rarefied flow computations using nonlinear model Boltzmann equations. *J. Comput. Phys.* **120** (2), 323–339.
- YU, J., VUORINEN, V., KAARIO, O., SARJOVAARA, T. & LARMI, M. 2013 Visualization and analysis of the characteristics of transitional underexpanded jets. *Intl J. Heat Fluid Flow* **44**, 140–154.